

Solid State Structure-Reactivity Studies of Bixbyite-Fluorite Phases Belonging to the Scandium-Vanadium-Oxygen System

By

Golnaz Samandari

A Thesis submitted to the Faculty of Graduate Studies of
The University of Manitoba
in partial fulfilment of the requirements of the degree of

MASTER OF SCIENCE

Department of Chemistry
University of Manitoba
Winnipeg

Copyright © 2017 by Golnaz Samandari

Abstract

The main focus of this thesis is to study solid-state reaction pathways by controlling structures during the synthesis of scandium vanadium oxides. Besides the synthesis of structures involving different oxidation states, the stable phases were identified by means of *ex-situ* powder X-ray diffraction as well as *in-situ* high temperature oxidation. For the synthesis of $\text{Sc}_{4/3}\text{V}_{2/3}\text{O}_3$ ($\text{Sc}_2\text{VO}_{4.5}$) and Sc_2VO_5 optimized methods are presented for the formation of a cubic bixbyite-type and tetragonal phase, respectively. In an *ex-situ* study Sc_2VO_5 was obtained by oxidation of $\text{Sc}_{4/3}\text{V}_{2/3}\text{O}_3$ ($\text{Sc}_2\text{VO}_{4.5}$). A deeper understanding of the structural changes can be obtained by focussing on the sub-lattices throughout the reaction pathway.

The phase change from cation-disordered bixbyite $\text{Sc}_2\text{VO}_{4.5}$ to cation-ordered tetragonal Sc_2VO_5 was studied through oxidation in trace amounts of oxygen. Moreover, the oxidation of bi-phasic samples of $\text{Sc}_{4/3}\text{V}_{2/3}\text{O}_3$ ($\text{Sc}_2\text{VO}_{4.5}$) and Sc_2VO_5 clearly indicates the competition of thermodynamic and kinetic routes during heating. Thermodynamic and kinetic oxidation products were compared based on the high temperature *in-situ* oxidation as well as *ex-situ* experiments. The product of topotactic oxidation of bixbyite $\text{Sc}_{4/3}\text{V}_{2/3}\text{O}_3$ ($\text{Sc}_2\text{VO}_{4.5}$) crystallizes in a defect fluorite structure $\text{Sc}_{4/3}\text{V}_{2/3}\text{O}_{3+\epsilon}$, (= $\text{Sc}_2\text{VO}_{5+\delta}$). The oxidation of the $\text{Sc}_{4/3}\text{V}_{2/3}\text{O}_3$ ($\text{Sc}_2\text{VO}_{4.5}$) bixbyite phase results in the formation of the reconstructed tetragonal Sc_2VO_5 structure at high. This finding is contrasted with the low temperature topotactic oxidation resulting in a disordered defect fluorite phase. Moreover, the conventional solid state method was used to explore the possibility of obtaining tetragonal Sc_2VO_5 . The results showed that solid state methods might not be suitable for the preparation of Sc_2VO_5 .

Acknowledgments

I would like to thank my supervisor Prof. Mario Bieringer for his guidance and support throughout my Master research. I would like to thank my advisory committee members Prof. Georg Schreckenbach and Prof. Anton Chakhmouradian for their helpful supports. I would like to thank Prof. Chris Wiebe for the collaboration during my research.

I am extremely thankful to the generous funding I have received including the University of Manitoba Graduate Fellowship, Faculty of Science Scholarship, International Graduate Student Entrance Scholarship, Department of Chemistry awards. Faculty of Graduate Studies, Faculty of Science, Graduate Students Association and Chemistry Graduate Students Association. Thanks to the past and present members of the Bieringer research group: Joey Lussier, Dr. Shahid Shafi, Dr. Harlyn Silverstein, Fabian Simon, Diego Souza, Pierre-Olivier Ferko, Jenny Panchuk.

Last but not least, my sincere thanks to my family and friends for their unconditional supports.

Dedicated to my consciousness Ehsan Alishahi.

Contents

Contents

CHAPTER 1	1
INTRODUCTION.....	1
1.1 Literature Review	3
1.1.1 AVO_3 (A = Ln, Sc, In) Structures	3
1.1.1.1 Perovskite Structure	4
1.1.1.2 Bixbyite Structure	6
1.2 $ScVO_3$ and $InVO_3$ Bixbyite Phases.....	7
1.2.1 A_2VO_5 (A = Sc, In, Yb, Dy and Y) Structures	9
1.3 Solid State Synthesis Methods	13
1.4 Powder X-ray Diffraction.....	14
1.5 The Rietveld Method	17
1.6 Objectives of the Research	20
 CHAPTER 2.....	 22
EXPERIMENTAL METHODS.....	22
2.1 Synthesis of Materials.....	22
2.1.1 Synthesis of $Sc_2VO_{4.5}$	22
2.1.2 Synthesis of Sc_2VO_5 by Oxidation of $Sc_2VO_{4.5}$	22
2.1.3 Synthesis of Sc_2VO_5 by Conventional Solid State Method.....	23
2.2 Room Temperature Powder X-ray Diffraction	23
2.3 High Temperature <i>In-Situ</i> Powder X-ray Diffraction	24

2.4	Data Analysis: Rietveld Refinement	24
CHAPTER 3		25
SYNTHESIS AND REACTIVITY OF TETRAGONAL Sc₂VO₅		25
3.1	Synthesis and Structural Analysis of the Bixbyite Sc ₂ VO _{4.5}	25
3.2	Defect Fluorite Structure Sc ₂ VO _{5+δ} (0.00 ≤ δ ≤ 0.50).....	28
3.3	Synthesis and Structure of Tetragonal Sc ₂ VO ₅	31
3.4	<i>In-situ</i> Diffraction Studies of Sc ₂ VO ₅ Formation in O ₂ Traces.....	39
3.5	Reductive Formation of Sc ₂ VO ₅	43
3.6	Solid State Direct Synthesis of Sc ₂ VO ₅	45
3.7	<i>In-situ</i> High Temperature Oxidation of a Bi-phasic Sample of Sc ₂ VO _{4.5} and Tetragonal Sc ₂ VO ₅ in Air	47
CHAPTER 4		52
CONCLUSION		52
REFERENCES		56

List of Tables

Table 3-1: *Crystallographic details for bixbyite phase for $\text{Sc}_2\text{VO}_{4.5}$ at room temperature obtained from Rietveld refinements against powder X-ray diffraction pattern with $\lambda=1.540598\text{\AA}$, 1.544426\AA27*

Table 3-2: *Crystallographic details of defect fluorite $\text{Sc}_2\text{VO}_{5+\delta}$ from Rietveld refinements obtained from powder X-ray diffraction pattern with $\lambda= 1.540598 \text{\AA}$, 1.544426\AA30*

Table 3-3: *Crystallographic details of tetragonal Sc_2VO_5 obtained from Rietveld refinement against a obtained from powder X-ray diffraction pattern with $\lambda= 1.540598 \text{\AA}$, 1.544426\AA35*

Table 3-4: *Bond distances for tetragonal Sc_2VO_5 from Rietveld refinement obtained from powder X-ray diffraction pattern with $\lambda= 1.540598 \text{\AA}$, 1.544426\AA37*

List of Figures

Figure 1-1: Cubic perovskite structure ABO_3 with green = A cation , blue = B cation, and red = oxygen.....5

Figure 1-2: Cubic bixbyite structure with the 8b sites in dark blue, the 24d site in light blue and oxygen in red. The left figure illustrates the coordination polyhedral connectivity and the right figure highlights the two cation sites.7

Figure 1-3: Orthorhombic In_2VO_5 crystalizes in space group $Pnma$ (#62). Cation positions are illustrated as purple ($In-O_6$) and blue ($V-O_5$) polyhedra and oxygen positions as red spheres11

Figure 1-4: Volume per formula unit for A_2VO_5 system versus ionic radius. The monoclinic (S.G $C2/c$ and $P2_1/c$) structure, orthorhombic (S.G $Pnma$) and tetragonal (S.G $I-4$) are shown in the diagram. The error bars are smaller than the symbols.^{35,27,36}13

Figure 1-5: Illustration of Bragg’s law. Constructive interference is observed when the lower beam path is longer by an integer multiple of the X-ray wavelength. The d-spacing describing the separation of parallel planes can thus be determined by Bragg’s law.³⁷16

Figure 3-1: Rietveld plot of $Sc_2VO_{4.5}$ bixbyite. red = experimental, black line = best fit, blue line = difference. Bragg positions are shown as blue tick marks. The inset emphasizes the small superstructure peaks. (Note poor fit of the (231) bixbyite peak is an artifact due to W emission from the anode).26

Figure 3-2: $Sc_2VO_{4.5}$ cubic bixbyite crystal structure with space group $Ia-3$ (#206). Light blue = 24d cation site, dark blue = 8b cation site, red = 48e oxide site. Cation positions are illustrated in blue and oxygen positions are in red¹³. The size of spheres are not showing the ionic size, and cations are labeled for their positions in this figure.28

Figure 3-3: Rietveld refinement of the defect fluorite structure $Sc_2VO_{5+\delta}$ ($0.00 \leq \delta \leq 0.50$). Red = experimental data, black = best fit and blue = difference. The Bragg peaks are represented by blue solid tick marks.....29

Figure 3-4: $Sc_2VO_{5+\delta}$ cubic defect fluorite crystal structure in space group $Fm-3m$ (#225). Cation positions are illustrated in blue and oxygen positions are in red.....31

Figure 3-5: Ex-situ powder X-ray diffraction after heating 500mg of $Sc_2VO_{4.5}$ in 5 ppm O_2 in N_2 at $800^\circ C$. The indicated reaction times are total times. The disappearance of the starting material is followed with the (222) $Sc_2VO_{4.5}$ peak and the formation of the product is followed with the (123) Sc_2VO_5 peak.....32

Figure 3-6: Rietveld refinement of tetragonal Sc_2VO_5 against powder X-ray diffraction. Red symbols = experimental data, black line = best fit, blue line = difference, blue tick marks = Bragg positions. The upper set of tick marks corresponds to the impurity phase $ScVO_4$ (zircon) the lower set corresponds to tetragonal Sc_2VO_533

Figure 3-7: Refined tetragonal Sc_2VO_5 structure with two vanadium and three scandium sites. Green = $Sc(1)-O_6$, yellow = $Sc(2)-O_7$, turquoise = $Sc(3)-O_7$, dark blue = $V(1)-O_6$ and purple = $V(2)-O_4$. Panel a. emphasizes the 5 coordination polyhedra and their connectivity. Panel b. shows the same as panel a. as a stick and ball representation. Panel c. shows the entire structure using coordination polyhedra viewing down the b axis. Panel d. illustrates viewing down the c-axis with all coordination polyhedral. Panel e. only shows the scandium-oxygen polyhedra and panel f. displays only the vanadium-oxygen polyhedra.....34

Figure 3-8: Illustration of local coordination environments and bond distances in tetragonal Sc_2VO_5 as discussed in the text. Green = $Sc(1)-O_6$, yellow = $Sc(2)-O_7$, turquoise = $Sc(3)-O_7$, dark blue = $V(1)-O_6$ and purple = $V(2)-O_4$38

Figure 3-9: (a) High temperature powder X-ray diffraction contour plot following the oxidation of $Sc_2VO_{4.5}$ bixbyite in trace amount of oxygen from $25^\circ C$ to $1200^\circ C$ for $2\theta=18-65^\circ$. Data were

<i>collected in 25°C increments. (b) Individual selected range from 29.5° to 32.5° high temperature X-ray diffraction contour plot.</i>	<i>42</i>
Figure 3-10: <i>Contour plot of Sc₂VO_{5+δ} reduction in flowing H₂ during heating from 25 to 600°C with 25°C increments.</i>	<i>44</i>
Figure 3-11: <i>(a) Powder XRD patterns of Sc₂O₃, V₂O₃ and V₂O₅ at 500°C in vacuum for first heating (black) and its second heating at 1100°C in vacuum (red). Blue pattern shows the first heating of another try at 1000°C in vacuum while the green diffractogram is second heating at 1000°C. (b) Selected region of patterns to indicate the main phase belong to tetragonal Sc₂VO₅ shown by arrow, and peaks with Star marks represent monoclinic VO₂ and triangle marks are assigned to V₈O₁₅ phase.....</i>	<i>46</i>
Figure 3-12: <i>(a) High temperature powder X-ray diffraction contour plot following the oxidation of Sc₂VO_{4.5} bixbyite and the tetragonal Sc₂VO₅. Data were collected in 5°C increments. (b) Individual in-situ powder X-ray diffractograms between 600°C and 1000°C emphasizing the phase evolution during oxidation in air. The grey double headed arrows emphasize the peak broadening for the fluorite phase up to 900°C. All relevant phases are indicated in figures 3-5 (a) and (b). ..</i>	<i>49</i>
Figure 3-13: <i>High temperature powder X-ray diffraction contour plot following the oxidation of Sc₂VO_{4.5} bixbyite and the tetragonal Sc₂VO₅ in trace amount of oxygen from 25°C to 1000 °C. Data were collected in 5°C increments. The step at 370°C is an experimental artifact due to an unexpected hold time at that temperature..</i>	<i>50</i>
Figure 4-1: <i>Flow chart of oxidation pathways for the Sc-V-O system as a function of temperature in trace amounts of oxygen as determined from ex-situ oxidation experiments starting with the Sc₂VO_{4.5} bixbyite phase.....</i>	<i>53</i>
Figure 4-2: <i>Phase existence during the in-situ oxidation in air of a biphasic Sc₂VO_{4.5} bixbyite and tetragonal Sc₂VO₅ sample. The intermediate phase is the Sc₂VO_{5+δ} fluorite phase and the final products are the ScVO₄ zircon structure and the Sc₂O₃ bixbyite structure.</i>	<i>55</i>

Chapter 1

INTRODUCTION

Solid state oxides are a large and diverse group of materials spanning a wide range of applications due to their tunable magnetic, electronic, optical and mechanical properties by means of different synthesis/processing methods and compositional variations¹. Commonly structure-property relations are cited as the first step for the design of novel functional materials². Understanding the function and processing of materials can be enhanced by focusing on structure-reactivity relations. This thesis is concerned with solid state oxides that are related to oxide ion conducting materials. Ion conductivity is closely related to the host structure and can be further investigated by probing the reactivity of such materials³. Oxide ion conductors are used as solid state electrolytes in Solid Oxide Fuel Cells (SOFCs)⁴. The majority of SOFCs are operated at approximately 900°C in order to increase oxide ion mobility to an acceptable level⁵. The current state-of-the-art SOFCs use yttria stabilized zirconia as the electrolyte⁵, a cubic oxide defect fluorite structure. In this thesis oxide defect structures related to the cubic fluorite phase will be explored for further use as model systems for oxide ion conductors. Particular emphasis will be on the stability and potential reaction products

of disordered defect fluorite structures in oxidizing and reducing atmospheres. Using redox active cations permits evaluating oxidative stabilities while commenting on oxide ion conductivities. This approach therefore relates structures and reactivities with materials properties⁶. This thesis explores the synthesis, structures and reactivities of $\text{Sc}_{4/3}\text{V}_{2/3}\text{O}_3$ ($= \text{Sc}_2\text{VO}_{4.5}$), $\text{Sc}_{4/3}\text{V}_{2/3}\text{O}_{3+\epsilon}$, ($= \text{Sc}_2\text{VO}_{5+\delta}$), and the ordered structure Sc_2VO_5 . Chapter 1 (Introduction) will provide a literature review of the known Sc-V phases, a brief description of solid state synthesis methods, powder diffraction and diffraction data analysis. Chapter 2 will provide the experimental details pertinent to the present work. Chapter 3 focuses on the tetragonal Sc_2VO_5 structure which will be explored with respect to the related bixbyite phase $\text{Sc}_{4/3}\text{V}_{2/3}\text{O}_3$ and the oxidized $\text{Sc}_{4/3}\text{V}_{2/3}\text{O}_{3+\epsilon}$ ($\epsilon \leq 2/3$) fluorite structures. After commenting on the synthesis and structure of Sc_2VO_5 its reactivity and potential formation pathway will be discussed. Conclusions stemming from this work will be provided in Chapter 4.

Investigating the formation pathways of crystalline inorganic solids will directly impact the understanding of solid state reactivities and will provide further insights into structure-property relationships. Such studies potentially lead to the development of synthetic and structural strategies for the design of novel functional materials⁷. The materials chosen in this thesis are model compounds for oxide ion conducting phases. Detailed structural studies including the evaluation of ion mobilities will be valuable for the design of SOFCs⁵ operating at high temperatures. Materials can be fine-tuned using a comprehensive synthetic tool kit and thus permit optimizing their physical properties such as magnetic, electronic and ion conducting characteristics⁸. The investigation of solid state reactivities will provide guidelines for the synthesis of those materials.

1.1 Literature Review

Vanadium is a 3d transition metal with oxidation states ranging from 0 to +5. Particularly common are V^{3+} , V^{4+} and V^{5+} in ternary and higher oxide phases. Notably vanadium has been reported to have multiple oxidation states in a number of structures⁹. The easily accessible redox chemistry of vanadium provides opportunities to generate diverse structures and to benefit from topotactic reaction pathways. Consequently vanadium-based containing oxide structures are excellent models for the investigation of structure–property–reactivity relations. A significant amount of research has been carried out on synthesis, characterization and physical properties of vanadates. Less work has been carried out on the reactivity of vanadates. In this section previous investigations on AVO_3 and A_2VO_5 are reviewed briefly.

1.1.1 AVO_3 (A = Ln, Sc, In) Structures

The formula ABO_3 encompasses a number of cation ordered and cation disordered structures. Notably the ordered structures include the perovskite ($CaTiO_3$), ilmenite ($FeTiO_3$), yttrium aluminum oxide ($YAlO_3$), lutetium manganese oxide ($LuMnO_3$), hexagonal perovskites ($BaMnO_3$) and calcium iridium oxide ($CaIrO_3$). Cation disordered structures can be based on the rhodium oxide (Rh_2O_3), corundum (Al_2O_3) and bixbyite ($c-Mn_2O_3$)^{10,11}. The observed structure type depends on the ionic radii and oxidation states of the A and B cations, as well as electronic effects (e.g. Jahn-Teller distortions). A number of compounds exist in two or more polymorphs, depending on the preparation method. Furthermore, phase transitions between many of these polymorphs are commonly observed as a function of temperature and pressure. Rare-earth vanadium oxides, AVO_3 (A = La – Lu) form orthorhombic perovskites and

have been studied extensively due to their intriguing magnetic and multiferroic properties, which are enhanced by complex low temperature structural phase transitions¹². ScVO_3 forms a cation disordered bixbyite-type structure, but can be also prepared as a metastable high pressure perovskite phase¹³. InVO_3 has also been reported as a metastable bixbyite phase that undergoes decomposition into its compound oxides at approximately 600 °C¹³. On one hand the diversity of structure types increases the complexity for these compounds. On the other hand the diversity also provides opportunities to fine-tune structures for specific practical applications and permits controlling the chemical reactivity and reaction pathways. The remainder of this chapter will give a brief introduction to perovskites and will further focus on introducing the structures directly related to this thesis. Furthermore, potentially competing phases will be considered as the reaction pathways are being investigated. Oxidation reactions are based on reduced bixbyite starting materials in an effort of generating fluorite type structures with varying degrees of cation and oxygen order.

1.1.1.1 Perovskite Structure

The perovskite structure is one of the most flexible structure types due to its compositional tolerance and a wide range of superstructures. ABO_3 perovskites have been investigated for applications as oxide and proton ion conductors and electrodes¹⁴, in fuel cells¹⁵, as sensors, as magnetic, optical and electronic materials, to mention only a few industrial applications. The versatile applications of perovskites are due to the ability to incorporate a wide range of cations, the possibility of mixed anion lattices and the formation of ordered superstructures.¹⁵ The ideal cubic perovskite structure consists of a 12-fold coordinated A cation (AO_{12}) and an octahedrally coordinated B cation (BO_6). The BO_6 units form a corner sharing octahedral network creating a large

cavity for the 12-fold coordinated A cation. The perovskite structure is illustrated in Figure 1-1.

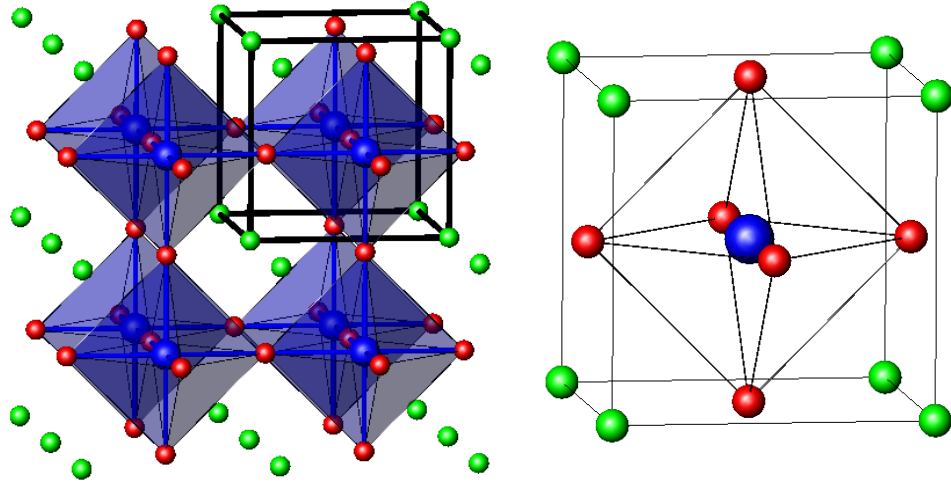


Figure 1-1: Cubic perovskite structure ABO_3 with green = A cation, blue = B cation, and red = oxygen.

The Goldschmidt Tolerance Factor, G_t ,¹⁶ provides a simple, yet good, first approximation for the prediction of perovskite structures solely based on ion size ratios as expressed in Equation 1-1:

$$G_t = \frac{d(A-O)}{\sqrt{2} d(B-O)} \quad \text{Equation 1-1}$$

where $d(A-O)$ is the A cation to oxygen and $d(B-O)$ is the B cation to oxygen bond distance based on their respective ionic radii. For $0.78 < G_t < 1.05$ perovskite structures are expected and will span a large range of distorted polymorphs derived from the cubic perovskite. The structure can undergo octahedral distortions, cooperative octahedral tilting¹⁷, orbital ordering, and cation substitutions in order to accommodate A- cations of different size¹⁸. Only for $G_t = 1.0$ the ideal cubic perovskite structure is expected. In the case of $G_t > 1.05$ the A cation is too large for the cavity and competing

phases will likely form. For $G_t < 0.78$ the A cavity formed by the B-O octahedral framework is too large for the actual A cation and a disordered phase is likely to form. For $G_t < 0.78$ cation disordered bixbyite phases such as ScVO_3 and InVO_3 are expected to form.¹⁹

1.1.1.2 Bixbyite Structure

The bixbyite structure is expected for ABO_3 compounds with similar A and B cation sizes and similar cation charges. The cubic bixbyite structure crystallizes in space group $Ia-3$ (#206) with two distinct cation sites ($8b$ and $24d$) and a fully occupied $48e$ oxygen site. All cations are coordinated by 6 anions. The $8b$ site forms a fairly regular octahedron whereas the $24d$ site is at the center of a rather distorted octahedral environment. All octahedra are linked through edge sharing and in case of the V^{3+} containing AVO_3 phases the small A^{3+} cation size is the primary reason for the formation of this disordered cation structure. The bixbyite structure is illustrated in Figure 1-2. For cations smaller than Lu^{3+} the bixbyite structure is observed for the AVO_3 phases, whereas Lu^{3+} and the larger trivalent rare-earth cations form perovskite structures.²⁰

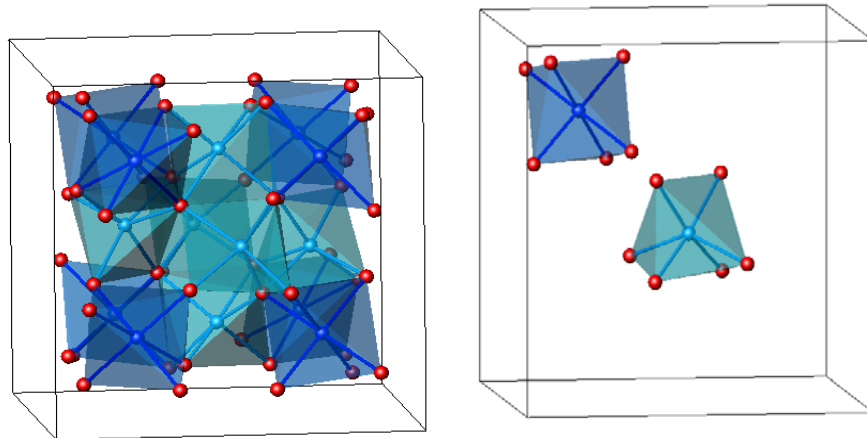


Figure 1-2: Cubic bixbyite structure with the 8b sites in dark blue, the 24d site in light blue and oxygen in red. The left figure illustrates the polyhedral connectivity and the right figure highlights the two cation sites.

1.2 ScVO₃ and InVO₃ Bixbyite Phases

In scandium vanadium systems, Alonso *et al.*²¹ studied the crystal structure at room temperature using high-resolution neutron powder diffraction and confirmed that ScVO₃ crystallizes in the cubic bixbyite structure. An intermediate phase of composition ScVO_{3.5}, containing V⁴⁺ cations, was isolated by isothermal annealing at 350°C in air. Shafi *et al.*¹³ identified the preparation and stability of ScVO_{3.5+x} fluorite and the equivalent oxidation product InVO_{3.5} by means of *ex-situ* methods. Thermogravimetric/differential thermal analysis and *in-situ* powder X-ray diffraction mapped the topotactic oxidation pathway for AVO₃ structures. Shafi *et al.*²² have shown the formation pathway of ScVO₄ zircon from ScVO₃ bixbyite and the synthetic method and stability of a novel intermediate product of the reaction with the generalized formula ScVO_{4-x}. In that study, the oxidation of ScVO₃ to ScVO₄, as well as two intermediates of composition ScVO_{3.5} and the novel phase ScVO_{4-x} were investigated. They reported that ScVO_{4-x} crystallizes in the zircon structure and ScVO₄.

x can only be obtained by oxidation of ScVO_3 or $\text{ScVO}_{3.5}$. It should be mentioned that the direct reduction of zircon-type ScVO_4 did not yield $\text{ScVO}_{3.5}$.²²

InVO_3 is interesting because the ionic radius of In^{3+} is between Sc^{3+} and Lu^{3+} . InVO_3 falls directly on the borderline separating the perovskite and bixbyite structures based on the Goldschmidt Tolerance Factor. InVO_3 crystallizes as bixbyite $Ia-3$ (#206) and was studied for the first time by Lundgren *et al.*²³. Based on the initial *in-situ* reduction of InVO_4 the first low temperature (~ 450 °C) InVO_3 bulk synthesis was developed. The preparation of InVO_3 is only possible during mild reduction of InVO_4 in a $\text{CO}:\text{CO}_2$ buffer gas at 450 °C. All other AVO_3 phases can be prepared by high temperature reduction in flowing hydrogen. The high temperature reductive synthesis of InVO_3 in strongly reducing atmospheres is prevented by the reduction of In^{3+} to indium metal and the decomposition of InVO_3 into its compound oxides (In_2O_3 and V_2O_3) above 600 °C. Another study by Shafi *et al.*¹³ reported the formation of the metastable oxide defect fluorite $\text{InVO}_{3.5+x}$ ($0 \leq x \leq 0.22$) using *in-situ* X-ray diffraction. The authors carried out the mild oxidation of InVO_3 in CO_2 at temperatures as low as 250 °C and obtained the cubic oxide defect fluorite structure $\text{InVO}_{3.5+x}$ that crystallizes in space group $Fm-3m$ (#225). Irreversible oxidation of $\text{InVO}_{3.5+x}$ is observed at 425 °C with the formation of the fully oxidized InVO_4 zircon type structure. Shafi *et al.* work emphasized the importance of the chemical reactivity of bixbyite and defect fluorite phases. Notably the oxidation reactions of ScVO_3 and InVO_3 did not result in oxygen excess in the bixbyite structure. The bixbyite phases oxidized directly to the defect fluorite structure $\text{AVO}_{3.5}$ with tetravalent vanadium. There is no evidence of V^{4+} in the original bixbyite phase with space group $Ia-3$. The defect fluorite phases oxidize to AVO_4 zircon phases upon further heating.

Lussier *et al.*²⁴ investigated the bixbyite oxide defect structures $\text{YPrO}_{3+\delta}$ ($0 \leq \delta \leq 0.46$). The redox chemistry of $\text{YPrO}_{3+\delta}$ is defined by the accessible praseodymium oxidation states of +3 and +4. Using high temperature *in-situ* powder X-ray diffraction topotactic oxygen insertion into the bixbyite structure was observed. The excess oxygen occupies the additional $16c$ (x,x,x) site and site splitting for the $8b$ cation is observed. The cation in the $8b$ position responds to the additional oxygen by moving off its original center position. The Y-Pr-O system permits to slowly oxidize the parent YPrO_3 bixbyite phase generating a range of partially oxidized bixbyite phases of composition YPrO_{3+x} ($0 \leq \delta \leq 0.46$). Lussier *et al.*²⁵ also investigated the solid solution $\text{Y}_{(2-x)}\text{Pr}_x\text{O}_{3+\delta}$ ($0.0 \leq x < 2.0$, $\delta \leq 1.0$) in an effort to obtain oxygen stoichiometries that are sufficient for the formation of oxide defect disordered fluorite structures. The praseodymium rich part of the solid solution allowed the formation of oxide defect structures with space group $Fm-3m$ (#225), whereas the yttrium rich part allowed the investigation of partially oxidized bixbyite structures. Their work identified that the site splitting of the $8b$ cation site will limit ion mobility in partially oxidized bixbyite phases, while the fully disordered fluorite structures are, as expected, appropriate for ion conduction applications.

1.2.1 A_2VO_5 (A = Sc, In, Yb, Dy and Y) Structures

The general composition A_2VO_5 suggests an intermediate oxidation state between the V^{3+} containing bixbyite structures AVO_3 which were discussed in the previous section and the V^{5+} containing orthovanadates AVO_4 (A = rare earth). The AVO_4 structures have attracted much attention among researchers because of their variable optical, magnetic, and electronic properties²⁶. Rare earth orthovanadates have many applications including as catalysts²⁷ and electrolytes²⁸. The majority of A_2VO_5 (V^{4+}) samples were initially byproducts of the synthesis of AVO_4 phases. This suggests that

there is a rich chemistry and structure field accessible between the bixbyite and the orthovanadate regimes. The following section provides a brief overview of the diverse A_2VO_5 ($A = Sc, In, Yb, Dy, Y$) compounds.

Four different structure types have been reported for A_2VO_5 including a tetragonal structure with space group $I-4$, an orthorhombic structure with space group $Pnma$ and two monoclinic structures with space groups $C2/c$ and $P2_1/c$.

The smallest A cation Sc^{3+} forms an ordered tetragonal fluorite structure. Cong *et al.*²⁹ reported a single crystal Sc_2VO_5 byproduct that was formed during the synthesis of neodymium doped $ScVO_4$ using the floating zone method. Cong *et al.* reported Sc_2VO_5 in space group $I-4$ (#82) with $Z = 10$ as an ordered fluorite defect structure with Sc^{3+} and V^{4+} cation ordering. The very small X-ray scattering contrast between Sc and V raises questions about the ordering of Sc and V in that structure. Notably V^{4+} is located in a fairly large octahedral site and in a smaller tetrahedral position based on the single crystal X-ray structure refinement of Cong *et al.*²⁹ The assigned V^{4+} should probably be reevaluated considering the very different coordination environments in those two different sites. It should also be mentioned that Mikhailov *et al.*³⁰ reported Sc_2VO_5 already in 1975 and indexed a powder X-ray diffraction pattern on a different tetragonal cell with $Z = 8$. Mikhailov *et al.*³⁰ prepared polycrystalline Sc_2VO_5 by direct reaction of Sc_2O_3 and VO_2 in a sealed tube. Unfortunately no details regarding the structure were provided in the original publication. To date no physical properties of Sc_2VO_5 have been published.

In_2VO_5 crystallizes in the cation ordered orthorhombic In_2TiO_5 structure type. The earliest report of In_2VO_5 dates back to 1975. Senegas *et al.*³¹ grew single crystals of In_2VO_5 and the isostructural compound In_2TiO_5 . In_2VO_5 crystallizes in the

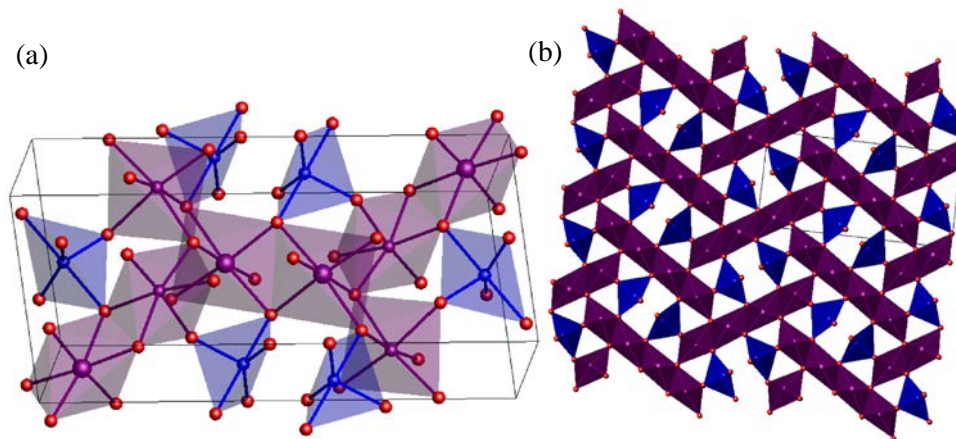


Figure 1-3: Orthorhombic In_2VO_5 crystallizes in space group $Pnma$ (#62). Cation positions are illustrated as purple ($\text{In}-\text{O}_6$) and blue ($\text{V}-\text{O}_5$) polyhedra and oxygen positions as red spheres.

orthorhombic space group $Pnma$ (#62) with cell parameters $a = 7.232 \text{ \AA}$, $b = 3.468 \text{ \AA}$, $c = 14.82 \text{ \AA}$ and $Z = 4$. In^{3+} is octahedrally coordinated in two distinct crystallographic sites and forms one-dimensional tetrameric $(\text{In}_2\text{O}_4)_n^{2n-}$ ribbons via octahedral edge sharing. V^{4+} is fivefold coordinated in a trigonal bipyramidal fashion. The VO_5 units link the $(\text{In}_2\text{O}_4)_n^{2n-}$ ribbons via corners in all three dimensions. The In_2VO_5 phase has been reported both as polycrystalline and single crystal specimens multiple times as part of physical property studies including thermal and magnetic properties by Singh *et al.*³². Moller *et al.*³³ published magnetization, electrical resistivity, and nuclear-electron spin resonance data for In_2VO_5 and discovered an antiferromagnetic to ferromagnetic transition at low temperature. It should be noted that the A_2TiO_5 structures ($\text{A} = \text{La} - \text{Ho}, \text{Yb}$)^{34,35,36,12} crystallize in this structure type as well. This is the most commonly encountered A_2BO_5 structure type for B^{4+} cations. The structure of In_2VO_5 is illustrated and further explored in Figure 1-3. The fully cation ordered orthorhombic structure has two $\text{In}^{3+} 4c$ sites and one $\text{V}^{4+} 4c$ site. In Figure 1-3 (a) the InO_6 octahedra and $\text{V}-\text{O}_5$ trigonal bipyramids are indicated in the unit cell in purple and blue, respectively.

The structure of orthorhombic In_2VO_5 consists of edge-sharing $\text{In}-\text{O}_6$ octahedra. The $\text{V}-\text{O}_5$ polyhedra connect the ribbons of InO_6 via corner-sharing. The tetrameric slabs and VO_5 connectivity is illustrated in Figure 1-3 (b).

Monoclinic A_2VO_5 structures were reported by Kimani *et al.*³⁷ for the larger A^{3+} rare earth cations, Yb^{3+} , Dy^{3+} and Y^{3+} . Detailed single crystal structures were published for the hydrothermally ($T = 560^\circ\text{C}$) grown samples. Yb_2VO_5 , Dy_2VO_5 and Y_2VO_5 crystallize in space group $C2/c$ (#15) when grown using a carbonate mineralizer. The structure only has one vanadium site. The V^{4+} cation is tetrahedrally coordinated in this structure and links AO_6 and AO_7 polyhedra via edges and corners.

Dy_2VO_5 was also found in a second polymorph when synthesized at a lower temperature ($T = 440^\circ\text{C}$) using KF as a mineralizer. The second polymorph is also monoclinic and crystallizes in space group $P2_1/c$ (#14). The reader is directed to Kimani *et al.*³⁷ for additional details.

Figure 1-4 shows a summary of the A_2VO_5 structures on a simple structure map as a function of volume per formula unit plotted against A^{3+} cation radius. The limited number of entries in conjunction with a rich structural diversity for the vanadates is in stark contrast to the larger number of equivalent A_2TiO_5 compounds that are found to form only one structure, namely the In_2TiO_5 structure. In particular the single points corresponding to space groups $I-4$ and $Pnma$ among the A_2VO_5 compounds illustrate that more work is required in order to rationalize those structures. Figure 1-4 shows that the $C2/c$ structures follow a linear volume increase with increasing A^{3+} ionic radius³⁷. For Sc_2VO_5 and In_2VO_5 the volume per formula unit does not follow the linear volume increase but their volumes are consistent with respect to their A^{3+} ionic radii. Surprisingly the $P2_1/c$ structure of Dy_2VO_5 is significantly denser than the $C2/c$

polymorph . This also poses the question if other compositions can be prepared as the $P2_1/c$ polymorph.

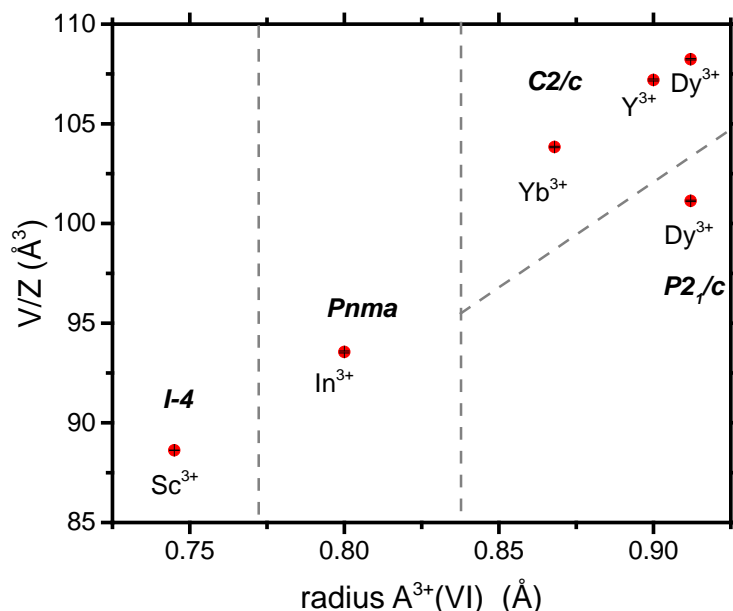


Figure 1-4: Volume per formula unit for A_2VO_5 system versus ionic radius. The monoclinic ($C2/c$ and $P2_1/c$), orthorhombic ($Pnma$) and tetragonal ($I-4$) structure fields are shown in the diagram. The error bars are smaller than the symbols.^{37,29,33}

1.3 Solid State Synthesis Methods

Solid state materials can be synthesized by using different techniques in inorganic chemistry. These techniques include high-temperature solid-state reactions and lower temperature reactions involving hydrothermal, sol-gel methods, and chimie douce or soft chemistry. The above mentioned methods make the systematic study of structure-property relationships possible and are important methods for designing materials.³³

Among these methods, the solid state reaction or “ceramic” method is the simplest and oldest method for the preparation of solid materials. Starting materials are mixed/ground together as powders, pressed into pellets and heated for extended periods. Reaction temperatures are kept below the melting temperature and the phase

formation consequently relies on ion diffusion across grain boundaries. The slow diffusion processes in solids render the “ceramic” method a slow synthesis route. Repeated grinding and heating may lead to single phase products. This is still the most common solid state synthesis method and often results in thermodynamically stable products. Most of the new high T_c superconductors were first prepared by this method³⁸. The main disadvantage of the ceramic method is the slow reaction between ingredients even when they are mixed together properly³⁸.

1.4 Powder X-ray Diffraction

Solid state materials can be classified as crystalline or amorphous. The crystalline state assumes long-range periodic structures that can be comprehensively described by their smallest repeating unit, the unit cell. In contrast amorphous or vitreous materials are defined by their short range order but lack of long range periodicity. Diffraction methods are excellent structural evaluation tools and are particularly powerful for the description of crystalline phases. Amorphous phases can be explored with diffraction methods as well but the results are usually more ambiguous than for crystalline structures.

Diffraction methods commonly use X-rays, neutrons and electrons as probes. X-rays and electron beams scatter from electron density in the investigated structure and are easily accessible in laboratory settings. In contrast neutrons scatter either from nuclei or from unpaired electrons in the structures. Neutron diffraction equipment is only available at large facilities such as nuclear research reactors or spallation neutron sources, which are located at particle accelerator laboratories. X-rays are the most applicable and accessible probe of all three mentioned probes. Routine phase identification and

structure determination using X-ray diffraction can be carried out in a reliable and expedient fashion.

Structures can be determined by either single crystal X-ray diffraction or powder X-ray diffraction. While single crystal diffraction is less ambiguous than powder diffraction, for structure determinations single crystals are often not available or do not properly describe a powder material. Powder X-ray diffraction is a fast and reliable method for the identification of crystalline structures and can be used for detailed structure determination by means of the Rietveld method (section 1-5). The Rietveld analysis is significantly more complex than single crystal diffraction analysis due to overlapping peaks in powder diffraction patterns.

When an X-ray beam strikes a sample diffraction occurs due to the repetition of diffracting planes described by their respective Miller indices. Bragg's law (Equation 1-2) relates the separation, d , of the diffracting planes with the X-ray wavelength λ , and the diffraction angle θ .

$$\lambda = 2d \sin \theta \qquad \text{Equation 1-2}$$

Figure 1-5 illustrates the geometric conditions for the interaction between X-rays and a pair of parallel atomic planes separated by distance d . The incoming parallel beams form the angle θ with the two parallel planes. The diffracted X-rays will be amplified due to constructive interference that results in an intensity maximum. Consequently, the path length difference of the two X-ray waves needs to be an integer multiple of the wavelength.^{33,39}

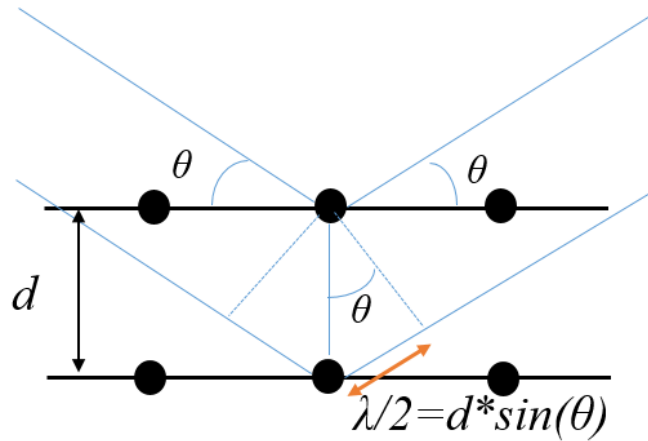


Figure 1-5: Illustration of Bragg's law. Constructive interference is observed when the lower beam path is longer by an integer multiple of the X-ray wavelength. The d -spacing describing the separation of parallel planes can thus be determined by Bragg's law.⁴⁷

X-ray diffraction maps the electron density in the diffracting sample. The intensity, I_{hkl} , of a diffraction peak is proportional to the square of the structure factor, F_{hkl} , as expressed in Equation 1-3:

$$I_{hkl} \propto |F_{hkl}|^2 \quad \text{Equation 1-3}$$

The structure factor F_{hkl} is the resultant of all scattering amplitudes of all atoms in the unit cell and is described in Equation 1-4.:

$$F_{hkl} = \sum_{j=1}^n g_j b_j f_j(2\theta) \exp[2\pi i(hx_j + ky_j + lz_j)] \quad \text{Equation 1-4}$$

Where hkl are the Miller indices, g_j is the occupancy factor, b_j is the temperature factor and $f_j(2\theta)$ which is the diffraction angle dependent form factor of atom/ion j . The terms x_j , y_j and z_j are the fractional coordinates of atom/ion j . The summation is carried out over the entire unit cell. The form factor is a function of the electron density of the scattering center with neighboring elements having very similar form factors. The form factors are diffraction angle dependent with the highest scattering power at $\sin\theta/\lambda = 0$.⁴⁰

The combination of Bragg's law and the structure factor equation provides almost unique powder diffraction patterns for different structures and compositions. Consequently, a powder diffractogram can serve as a fingerprint of a crystalline phase. Phase identification on the basis of diffraction patterns is therefore possible and one of the most common, albeit least sophisticated, applications. Furthermore powder diffraction patterns can be calculated using Bragg's law, the structure factor equation, corrections for peak multiplicities, absorption and Lorentz-polarization effects. A wide variety of peak functions is available in order to describe sample aberrations and instrumental contributions to the diffraction process. The peak full width half maximum, FWHM, as a function of the diffraction angle, can be described with the Cagliotti⁴¹ function (Equation 1-5), which has three refineable parameters, u , v and w .

$$(FWHM)^2 = u (\tan(\theta))^2 + v \tan(\theta) + w \quad \text{Equation 1-5}$$

After subtracting the instrumental broadening, the sample contributions to the peak widths can be assessed. This gives insight into domain size and stress-strain effects. The Scherrer equation describes the spherical crystalline domain size, D , based on the sample contribution to the integral peak breadth β . Equation 1-6 describes the simple Scherrer equation⁴²:

$$D = \frac{K\lambda}{\beta \cos \theta} \quad \text{Equation 1-6}$$

The shape factor K is usually given the numerical value 0.9, λ is the X-ray wavelength and θ is the diffraction angle in radians.

1.5 The Rietveld Method

Detailed crystallographic structures can be obtained from powder diffraction data via the Rietveld method. Since powder diffraction data do not consist of well separated

diffraction peaks the Rietveld method uses individual diffraction data points and minimizes the difference between the experimental data and the data generated by the crystallographic model. Consequently, a starting model that is reasonably close to the actual structure is required in order to conduct a Rietveld refinement.

The Rietveld algorithm is based on a least squares minimization. Considering the experimental profile $y_{i,obs}$ and the calculated profile $y_{i,calc}$ points the following non-linear minimization function is used.⁴³

$$F = \sum_i w_i \left(y_{i,obs} - \frac{1}{c} y_{i,calc} \right)^2 \quad \text{Equation 1-7}$$

where w_i and c are weighting factors and the sum is carried out over all profile points. In other words, when minimizing the function F the difference between the experimental and refined intensities will be the least value.

The quality of the Rietveld fit is assessed with a number of statistical descriptors and R-values describing the residuals. Some of the commonly used residuals that need to be minimized are: R_p (profile residual), R_{wp} (weighted profile residual), R_{exp} (expected profile residual), χ^2 (goodness of fit) and the R_{Bragg} (Bragg factor). In order to determine the fitting quality, the profile residual or R_p can be used to compare the observed and calculated intensities. In contrast R_{wp} using a weighting factor for comparing the experimental and simulated patterns. The estimation of the quality of the fit will be determined by χ^2 which is the correlation between R_{wp} and R_{exp} . In addition to the R-values the quality of the fit is usually judged by the Rietveld plot, the difference curve (between model and actual data) is usually a good guide for the refinement strategy. The following equations (Equation 1-8 to Equation 1-11)⁴⁴ are summarizing the expressions for the R-values and χ^2 .⁴⁵

$$R_p = \frac{\sum_{i=1}^n |Y_{oi} - Y_{ci}|}{\sum_{i=1}^n Y_{oi}} \times 100\% \quad \text{Equation 1-8}$$

$$R_{wp} = \left[\frac{\sum_{i=1}^n w_i (Y_{oi} - Y_{ci})^2}{\sum_{i=1}^n w_i (Y_{oi})^2} \right]^{\frac{1}{2}} \times 100\% \quad \text{Equation 1-9}$$

$$R_{exp} = \left[\frac{n - p}{\sum_{i=1}^n w_i (Y_{oi})^2} \right]^{\frac{1}{2}} \times 100\% \quad \text{Equation 1-10}$$

$$\chi^2 = \frac{\sum_{i=1}^n w_i (Y_{oi} - Y_{ci})^2}{\sum_{i=1}^n Y_{oi}} = \left[\frac{R_{wp}}{R_{exp}} \right]^2 \quad \text{Equation 1-11}$$

The refineable parameters in a Rietveld analysis can be partitioned into two broad groups:

(1) Sample specific parameters and (2) instrumental parameters. The sample specific parameters are at the center of the analysis as those provide a description of the actual structure. Those will eventually permit the determination of coordination environments, bond lengths and angles and will provide insights into order and disorder. The sample related parameters are the unit cell dimensions, atomic positions, site occupancies and thermal parameters (Debye-Waller factors). The instrumental parameters include the scale factor, the background parameters, the zero point parameter for the detector position and the asymmetry parameters. Furthermore, the peak shape including the peak function and the U, V and W parameters and preferred orientation parameters are commonly treated as instrumental or global parameters but are actually convoluted parameters that combine sample and instrument contributions. For example, the empirical Caglioti function (Equation 1-12) can be used to fit the peak widths with no real physical meaning, this means that those parameters provide an empirical resolution function as part of the refinement.⁴¹

$$H_k^2 = u \tan^2 \theta_k + v \tan \theta_k + w \quad \text{Equation 1-12}$$

where H is the full width at half maximum intensity at angle θ . The parameters u , v , w can be refined. The Caglioti function is empirical but the peak widths actually can provide further information on domain sizes and sample strain.

During a Rietveld refinement the crystallographic and instrumental parameters are determined and the resulting final refined structure should be physically meaningful. The Rietveld fits can be visually inspected and a mismatch can often be traced to specific parameters that will then be addressed during further refinement cycles. There is no general process for the order of parameters to be added to the refinement. The decision which parameters to refine and in what order depends on the individual data sets and crystallographic questions to be answered. Conducting Rietveld refinements on multiphase samples is common and a properly set up model and refinement strategy will allow for quantitative phase determination as well. The refinement results can provide important input for setting up the chemical reactions that eventually describe the reaction pathway. Therefore the Rietveld method is not only of crystallographic concern, it is also a tool for a deeper understanding of chemical processes in crystalline materials.

1.6 Objectives of the Research

Despite the interesting structural details of the vanadium-scandium-oxide system the physical properties of the tetragonal phase Sc_2VO_5 are not known. This is likely due to challenges with the synthesis of this phase, which is in competition with disordered phases and because Sc_2VO_5 can decompose into ScVO_4 and Sc_2O_3 . Mikhailov *et al.*³⁰ reported the first polycrystalline sample of Sc_2VO_5 prepared by heating a mixture of Sc_2O_3 and VO_2 in a sealed tube. Sc_2VO_5 was not reported again until the work of Cong *et al.*²⁹. Cong *et al.* obtained Sc_2VO_5 accidentally when preparing neodymium doped

scandium orthovanadate single crystals (Nd: ScVO₄) using the floating zone method. In that study, the zircon-type ScVO₄, bixbyite-type Sc₂O₃, and tetragonal Sc₂VO₅ were obtained. That work also clearly indicated the formation of competing phases. The current research focuses on the structure and explores in particular potential preparation methods for the ordered Sc₂VO₅ structure. The different oxidation states of vanadium account for the diversity of phases and structures in the Sc-V-O system. Investigation of such structures might provide us with more insight into solid state chemistry.

Chapter 2

EXPERIMENTAL METHODS

2.1 Synthesis of Materials

2.1.1 Synthesis of $\text{Sc}_2\text{VO}_{4.5}$

$\text{Sc}_2\text{VO}_{4.5}$ was prepared from stoichiometric amounts of Sc_2O_3 and V_2O_3 by the conventional solid state method. Phase pure V_2O_3 was prepared by reduction of V_2O_5 (CERAC, 99.9%) at 1100°C for 15 hours in flowing pure H_2 . Sc_2O_3 (Alfa Aesar, 99.995%) and V_2O_3 were ground in acetone and heated at 1500°C for 96 hours with two intermediate grindings according to Equation 2-1 and Equation 2-2.



The light brown product was phase pure bixbyite with composition of $\text{Sc}_2\text{VO}_{4.5}$.

2.1.2 Synthesis of Sc_2VO_5 by Oxidation of $\text{Sc}_2\text{VO}_{4.5}$

Polycrystalline tetragonal Sc_2VO_5 with an intermediate oxidation state of vanadium (V^{4+}) was synthesized by oxidation of the $\text{Sc}_2\text{VO}_{4.5}$ bixbyite phase under mildly oxidizing conditions. This was accomplished by oxidizing $\text{Sc}_2\text{VO}_{4.5}$ in trace amounts of oxygen (≈ 5 ppm) in N_2 at 800°C according to Equation 2-3.



2.1.3 Synthesis of Sc₂VO₅ by Conventional Solid State Method

The synthesis of Sc₂VO₅ was attempted by direct reaction of stoichiometric amounts of Sc₂O₃ and V₂O₃ and V₂O₅ (CERAC, 99.9%) which were ground in acetone and heated at temperature range 700°C-1000°C in static vacuum for 24 hours according to Equation 2-4.



2.2 Room Temperature Powder X-ray Diffraction

Room temperature powder X-ray diffraction measurements were carried out on samples using a PANalytical X'Pert Pro diffractometer in Bragg-Brentano configuration. The diffractometer used Cu-K $\alpha_{1,2}$ ($\lambda(\text{K}\alpha_1) = 1.540598 \text{ \AA}$, and $\lambda(\text{K}\alpha_2) = 1.544426 \text{ \AA}$) radiation and was equipped with a diffracted beam Ni-filter and an X'Celerator detector. The incident beam optics used 0.04 rad soller slits, 1° divergence slit, 10 mm mask and 2° anti scatter slit. The diffracted beam optics included a 3.4 mm anti scatter slit, 0.04 rad soller slits and a nickel K β filter. The X'Celerator is an ultra-fast X-ray RTMS (Real Time Multiple Strip) detector using 128 detector strips. Samples were mounted as acetone slurries on a 30 mm diameter silicon zero background holder. After grinding in acetone, samples are mounted as a thin layer on the sample holder. Standard measurements were conducted over an angular range $10^\circ \leq 2\theta \leq 120^\circ$ using 0.0167° steps. The preliminary data analysis was carried out with the X'Pert High Score Plus software (version 2.1.0) including phase identification (PDF 2003), indexing and space group determination.

2.3 High Temperature *In-Situ* Powder X-ray Diffraction

The PANalytical X'Pert Pro diffractometer equipped with an Anton Paar HTK2000 high temperature chamber was employed for *in-situ* high temperature powder X-ray diffraction experiments. Finely ground powders were mounted as acetone slurries directly on the platinum strip heater. The furnace temperature is within $\pm 5^{\circ}\text{C}$ of the set temperature between room temperature and 1200°C . Diffraction experiments were carried out between room temperature and 1200°C using different temperature increments as required by the sample. Different atmospheres of oxidizing (O_2 , impure N_2), reducing (H_2 , CO), and inert gases (N_2 and Ar) as well as a dynamic vacuum were used for the high temperature diffraction experiments. Diffraction data were collected isothermally with constant heating increments between measurement temperatures. The specific heating ramps and measurement times are listed with the actual diffraction data in the results section. Measurements were carried out during heating and cooling where required.

2.4 Data Analysis: Rietveld Refinement

The powder X-ray diffraction data were analyzed by the Rietveld method using the FullProf 2008 package. Detailed crystallographic information was obtained from the Rietveld refinements using laboratory based powder X-ray diffraction data. The refined parameters included the scale factor, unit cell parameters, atomic coordinates, temperature factors, background parameters, the zero point, sample displacement, peak shape function, the resolution function and peak asymmetry parameters. Additional details for the specific refinements are listed in the data tables in the results section.

Chapter 3

SYNTHESIS AND REACTIVITY OF TETRAGONAL Sc_2VO_5

3.1 Synthesis and Structural Analysis of the Bixbyite $\text{Sc}_2\text{VO}_{4.5}$

Phase pure bixbyite $\text{Sc}_2\text{VO}_{4.5}$, obtained by solid state reaction of stoichiometric amounts of Sc_2O_3 and V_2O_3 at 1500°C , crystallizes in space group $Ia-3$ (#206). Based on previous neutron diffraction data of ScVO_3 ¹³ this phase is expected to be cation disordered on the $8b$ and $24d$ sites. Figure 3-1 shows the powder X-ray diffraction based Rietveld plot of the bixbyite structure and Table 3-1 summarizes the structural details including selected bond distances of $\text{Sc}_2\text{VO}_{4.5}$. The Rietveld refinement of the $\text{Sc}_2\text{VO}_{4.5}$ structure was carried out with a total of 29 parameters including unit cell parameters, all atomic positions, the scale factor, zero point, peak shape parameters and Debye-Waller temperature factors were refined.

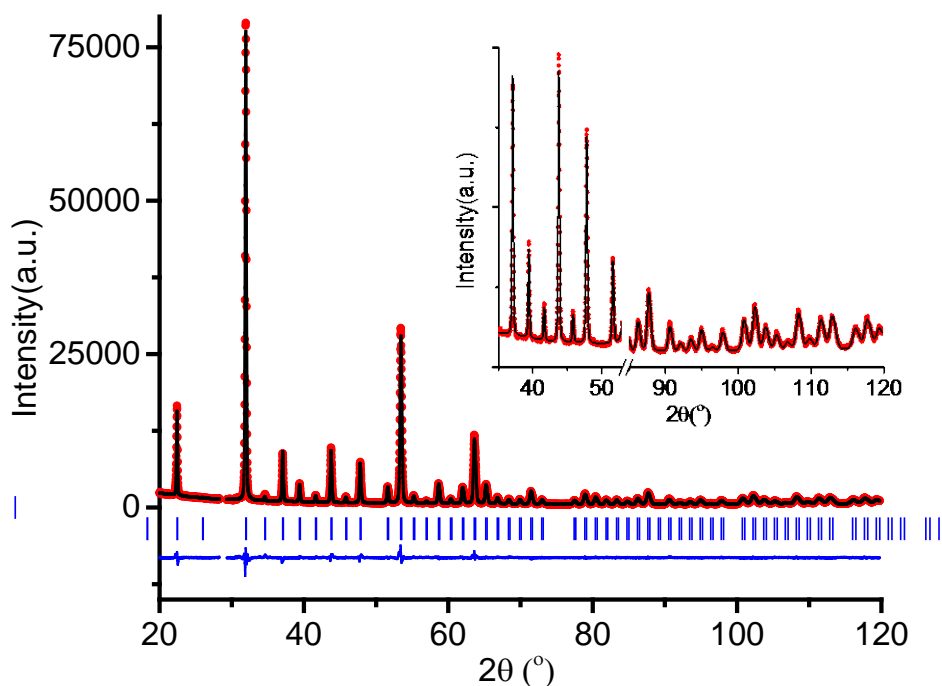


Figure 3-1: Rietveld plot of $Sc_2VO_{4.5}$ bixbyite. red = experimental, black line = best fit, blue line = difference. Bragg positions are shown as blue tick marks. The inset emphasizes the small superstructure peaks. (Note: The poor fit of the (231) bixbyite peak is an artifact due to W emission from the anode).

The $Sc_2VO_{4.5}$ bixbyite structure is illustrated in Figure 3-2. $Sc_2VO_{4.5}$ crystallizes in the cubic space group $Ia-3$ (#206) and consists of edge and corner sharing $(Sc^{3+}/V^{3+}) - O_6$ polyhedra. The cations are assumed to be randomly distributed over the two distinct, $8b$ and $24d$ sites¹³. The $8b$ cation site is octahedrally coordinated whereas the $24d$ cation is located in a distorted 6-fold coordinated oxide polyhedron that can be derived from a cubic coordination after removing two oxide anions across a face diagonal.¹³ The oxide anions are located in the fully occupied $48e$ site.

Table 3-1: Crystallographic details for bixbyite phase for $\text{Sc}_2\text{VO}_{4.5}$ at room temperature obtained from Rietveld refinements against powder X-ray diffraction pattern with $\lambda = 1.540598 \text{ \AA}$, 1.544426 \AA .

Composition		$\text{Sc}_2\text{VO}_{4.5} = \text{Sc}_{4/3}\text{V}_{2/3}\text{O}_3$	
Space group		$Ia-3$ (No. 206)	
Unit cell	a (Å)	9.6971(1)	
Volume	V (Å ³)	911.87(2)	
Number of formula units	Z	16	
Atomic position		B_{iso} (Å ²)	
$\text{Sc}^{3+}/\text{V}^{3+}$ (8b) (1/4,1/4,1/4)			-0.47(2)
$\text{Sc}^{3+}/\text{V}^{3+}$ (24d) (x,0,1/4)	x	0.96471(4)	-0.47(2)
O (48e) (x,y,z)	x	0.3914(1)	-0.90(3)
	y	0.1568(1)	
	z	0.3808(2)	
d (Sc(1)/V(1))-O (Å)	6 * 2.075(1)		
d (Sc(2)/V(2))-O (Å)	2 * 2.103 (1)		
	2 * 2.043 (1)		
	2 * 2.146 (2)		
X-ray ($\lambda=1.540598 \text{ \AA}$)	χ^2	R_{wp}	R_{p}
	3.811	8.37	7.72
# of Parameters	29		

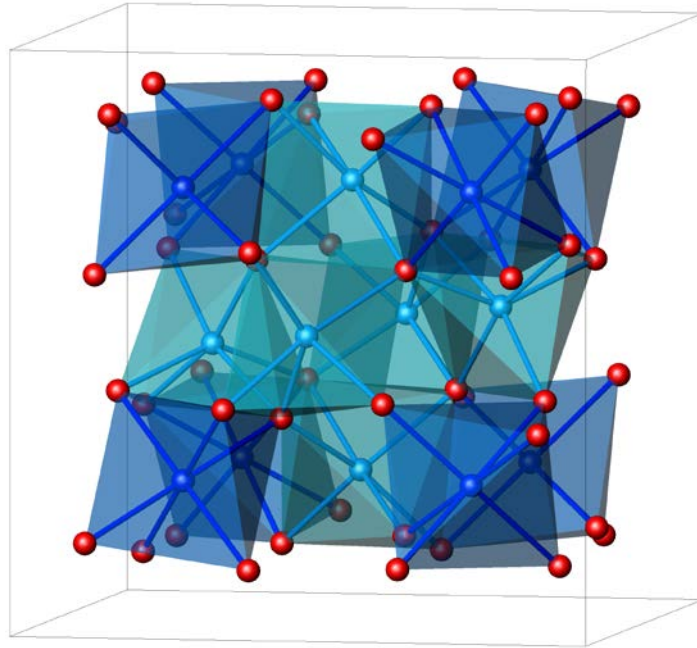


Figure 3-2: $Sc_2VO_{4.5}$ cubic bixbyite crystal structure with space group $Ia-3$ (#206). Light blue = 24d cation site, dark blue = 8b cation site, red = 48e oxide site. Cation positions are illustrated in blue and oxygen positions are in red¹³.

In the fluorite structure the cations form a cubic close packed sublattice and the anions occupy all tetrahedral positions. In such a configuration, anions occupy tetrahedral interstitials. Removing either 1 anion or 2 anions in an ordered fashion leads to the formation of pyrochlore or bixbyite phases, respectively.¹³

3.2 Defect Fluorite Structure $Sc_2VO_{5+\delta}$ ($0.00 \leq \delta \leq 0.50$)

$Sc_2VO_{4.5}$ can be oxidized topotactically to the defect fluorite structure $Sc_2VO_{5+\delta}$ ($0.00 \leq \delta \leq 0.50$) in flowing oxygen at temperatures as low as 350°C. This process is in agreement with the work published for the oxidation of $ScVO_3$ ¹³. The cubic fluorite structure is described in space group $Fm-3m$ (#225) with the cations located in the 4a site (0,0,0) and the oxide anions located in the 8c site ($\frac{1}{4}, \frac{1}{4}, \frac{1}{4}$). Figure 3-3 indicates excellent agreement between the refined structure and the experimental powder X-ray diffraction data. The crystal structure is illustrated in Figure 3-4 and the structural

details are provided in Table 3-2. Notably all bixbyite superstructure peaks are absent indicating cation disorder and oxide/defect disorder in space group $Fm-3m$. The dark green color of the sample suggests incomplete oxidation. Therefore it is proposed that a vanadium oxidation state between +4 and +5 has been obtained. In contrast, the fully oxidized phase is expected to be beige. The oxide defect concentration must be between 8.3% and 16.6% for $\delta = 0.5$ and 0.0, respectively. The oxide defect concentration in the present $Sc_2VO_{5+\delta}$ fluorite phase is approaching typical values used in solid state oxide ion conductors. The large temperature factors in $Sc_2VO_{5+\delta}$ suggest that the oxide anions in this cubic defect oxide structure are reasonably mobile.

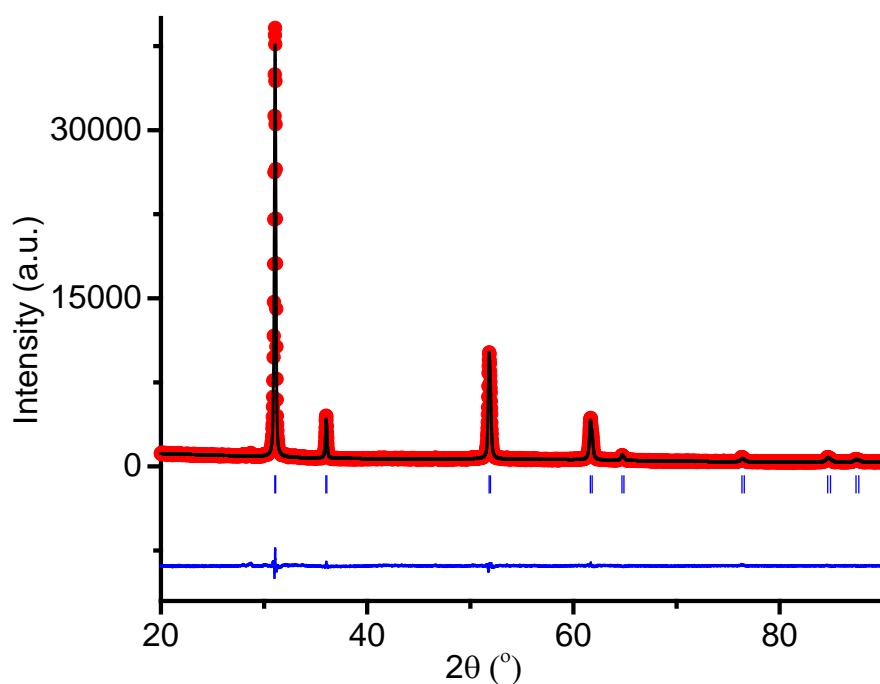


Figure 3-3: Rietveld refinement of the defect fluorite structure $Sc_2VO_{5+\delta}$ ($0.00 \leq \delta \leq 0.50$). Red = experimental data, black = best fit and blue = difference. The Bragg peaks are represented by blue solid tick marks.

Table 3-2: Crystallographic details of defect fluorite $Sc_2VO_{5+\delta}$ from Rietveld refinements obtained from powder X-ray diffraction pattern with $\lambda = 1.540598 \text{ \AA}$, 1.544426 \AA .

Composition		$Sc_2VO_{5+\delta} = Sc_{4/3}V_{2/3}O_{3+\epsilon}$	
Space group		$Fm-3m$ (No. 225)	
Unit cell	a (\AA)	4.9861(1)	
	V (\AA^3)	123.962(5)	
Number of formula units	Z	2	
Atomic position			$B_{iso}(\text{\AA}^2)$
$Sc^{3+} / V^{3+} (4a) (0,0,0)$	4a		4.4 (1)
O (8c) ($1/4, 1/4, 1/4$)	8c		11.0(3)
d (Sc/V-O) (\AA)	2.15905(3)		
X-ray ($\lambda=1.540598 \text{ \AA}$, 1.544426 \AA)	χ^2	R_{wp}	R_p
	2.343	9.24	10.5
# of Parameters	21		

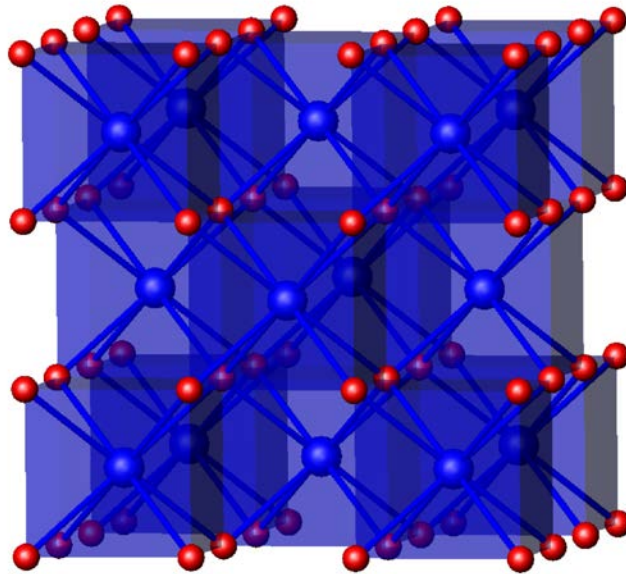


Figure 3-4: $Sc_2VO_{5+\delta}$ cubic defect fluorite crystal structure in space group $Fm-3m$ (#225). Cation positions are illustrated in blue and oxygen positions are in red.

3.3 Synthesis and Structure of Tetragonal Sc_2VO_5

The previously reported tetragonal phase Sc_2VO_5 has been obtained here for the first time by means of slow oxidation of the parent bixbyite $\text{Sc}_2\text{VO}_{4.5}$ at elevated temperatures. Using only traces of oxygen in nitrogen (approx. 5 ppm O_2) and heating the starting material to 800°C permits the formation of the tetragonal phase. Notably the sample preparation requires constant monitoring of the product. Due to the limited amount of oxygen provided during the slow oxidation, unreacted starting material is initially observed whereas extended heating periods may result in the zircon phase ScVO_4 due to over-oxidation. Figure 3-5 illustrates the slow oxidation of approximately 500mg of $\text{Sc}_2\text{VO}_{4.5}$ bixbyite phase in 5 ppm oxygen in nitrogen at 800°C . The tetragonal Sc_2VO_5 phase starts forming after 48 hours but even after 168 hours the starting material is still present.

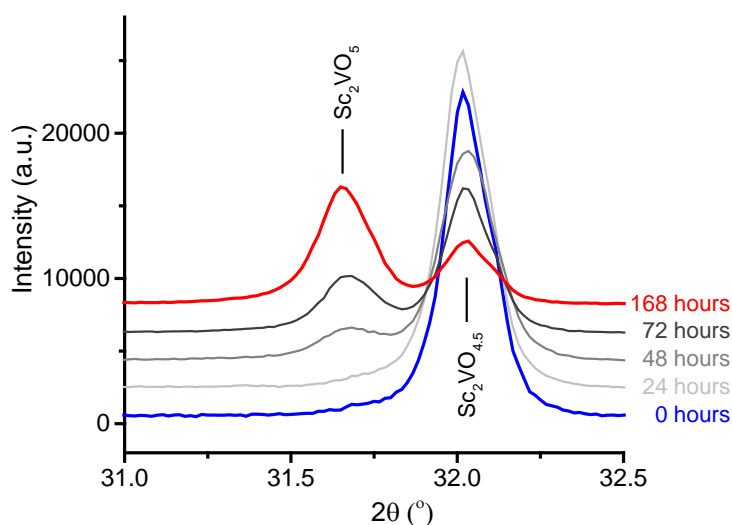


Figure 3-5: Ex-situ powder X-ray diffraction after heating 500 mg of $\text{Sc}_2\text{VO}_{4.5}$ in 5 ppm O_2 in N_2 at 800°C . The indicated reaction times are total times. The disappearance of the starting material is followed with the (222) $\text{Sc}_2\text{VO}_{4.5}$ peak and the formation of the product is followed with the (123) Sc_2VO_5 peak.

100 mg of $\text{Sc}_2\text{VO}_{4.5}$ were oxidized in 5 ppm O_2 in N_2 at 800°C resulting in tetragonal Sc_2VO_5 with a small ScVO_4 impurity within 24 hours. The structure of Sc_2VO_5 has been refined with the Rietveld method in space group $I-4$ (# 82) using the structure published by Cong *et al.*²⁹ as the initial model. The sample contains approximately 17% ScVO_4 impurity. The Rietveld analysis is complicated due to significant peak overlap for the two phases. The Rietveld plot is shown in Figure 3-6 and the crystallographic details are provided in

Table 3-3. The detailed structural evaluation of Sc_2VO_5 using X-ray diffraction suffers from the similar X-ray form factors of scandium and vanadium. The original publication by Cong *et al.*²⁹ identified cation ordering and assumed an oxidation state of +4 for vanadium which has also been reported to be located on two very differently coordinated cation sites.

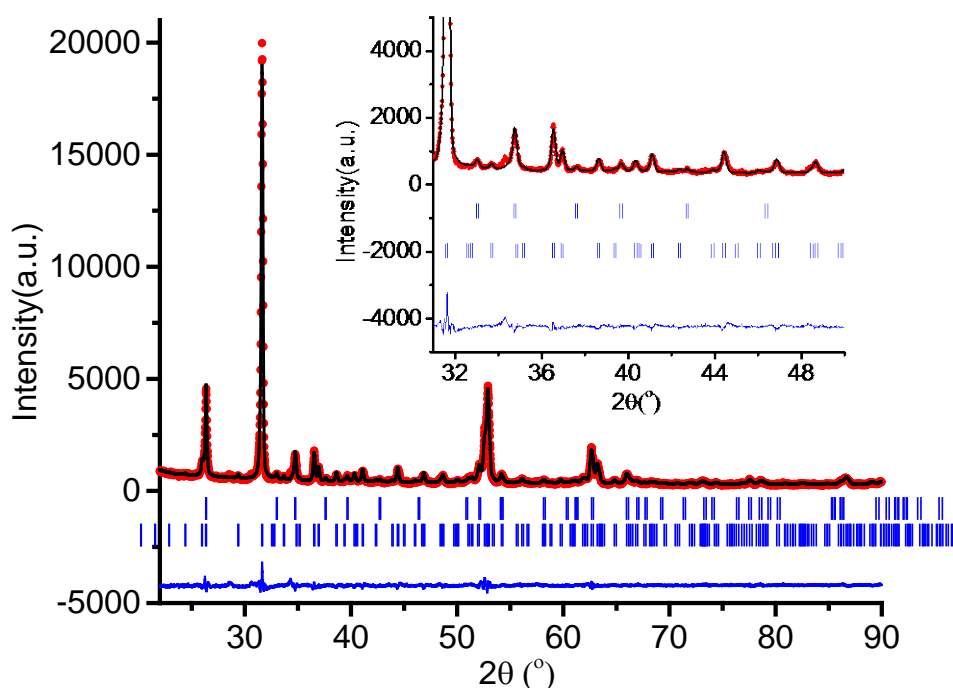


Figure 3-6: Rietveld refinement of tetragonal Sc_2VO_5 against powder X-ray diffraction data. Red symbols = experimental data, black line = best fit, blue line = difference, blue tick marks = Bragg positions. The upper set of tick marks corresponds to the impurity phase ScVO_4 (zircon) the lower set corresponds to tetragonal Sc_2VO_5 .

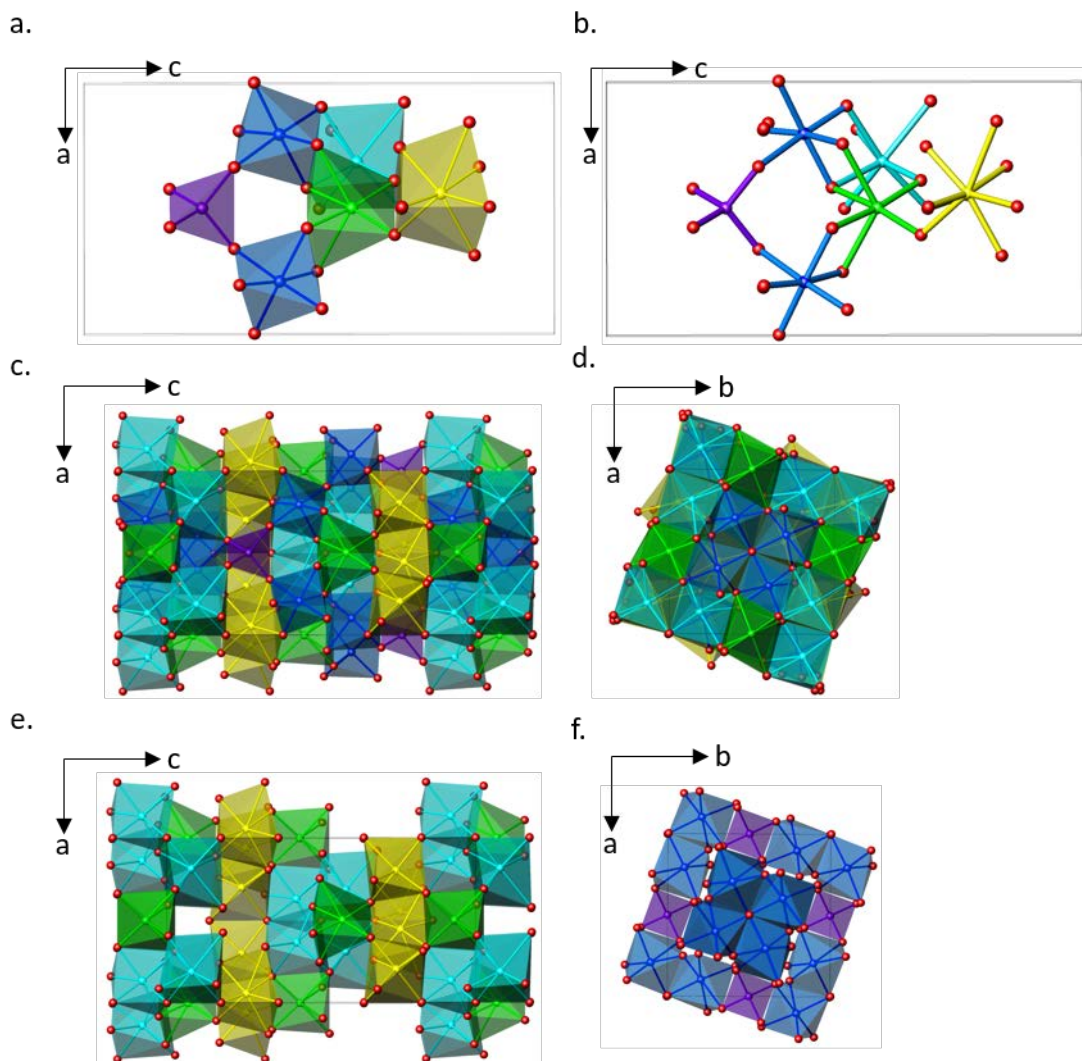


Figure 3-7: Refined tetragonal Sc_2VO_5 structure with two vanadium and three scandium sites. Green = $\text{Sc}(1)\text{-O}_6$, yellow = $\text{Sc}(2)\text{-O}_7$, turquoise = $\text{Sc}(3)\text{-O}_7$, dark blue = $\text{V}(1)\text{-O}_6$ and purple = $\text{V}(2)\text{-O}_4$. Panel a. emphasizes the 5 coordination polyhedra and their connectivity. Panel b. shows the same as panel a. as a stick and ball representation. Panel c. shows the entire structure using coordination polyhedra viewing down the b axis. Panel d. illustrates viewing down the c-axis with all coordination polyhedra. Panel e. only shows the scandium-oxygen polyhedra and panel f. displays only the vanadium-oxygen polyhedra.

Table 3-3: Crystallographic details of tetragonal Sc_2VO_5 obtained from Rietveld refinement against a obtained from powder X-ray diffraction pattern with $\lambda = 1.540598 \text{ \AA}$, 1.544426 \AA .

Space group					<i>I-4</i> (No. 82)
Unit cell		a (Å)		7.7786(5)	
		c (Å)		14.5982(11)	
		V (Å ³)		883.3(9)	
Number of formula units		Z		10	
Atom	Site	x	y	z	B _{iso} (Å ²)
V(1)	8g	0.9450(9)	0.1998(12)	0.2574(6)	1.77(6)
V(2)	2d	1.00000	0.50000	0.75000	1.77(6)
Sc(1)	4f	1.00000	0.50000	0.4314(7)	1.77(6)
Sc(2)	8g	0.9450(9)	0.1998(12)	0.2574(6)	1.77(6)
Sc(3)	8g	0.6234(10)	0.3143(12)	0.4203(5)	1.77(6)
O(1)	8g	1.09640	0.24850	0.50460	1.01(9)
O(2)	8g	0.83780	0.39150	0.34010	1.01(9)
O(3)	8g	0.81330	0.41830	0.52670	1.01(9)
O(4)	4e	1.00000	0.00000	0.63850	1.01(9)
O(5)	4e	1.00000	0.00000	0.17490	1.01(9)
O(6)	2d	0.50000	0.50000	0.50000	1.01(9)
O(7)	8g	0.73960	0.19100	0.67060	1.01(9)
O(8)	8g	1.07710	0.33790	0.68130	1.01(9)
X-ray ($\lambda=1.540598 \text{ \AA}$, 1.544426 Å)		χ^2		R _{wp}	R _p
		2.78		14.1	14.6
# of Parameters		44			

The bond distances for Sc_2VO_5 obtained from the present Rietveld refinement are listed in

Table 3-4 and are in agreement with the original single crystal structure. Figure 3-7 illustrates the refined structure of tetragonal Sc_2VO_5 . Figure 3-8 illustrates the metal-oxygen bond distances for the 5 different cation sites. The ordered defect fluorite superstructure has been discussed in detail by Cong *et al.*²⁹. The agreement of the Rietveld structure presented here and the original report is very good, however the oxide positions were not refined for the powder sample. The Sc(1)-O₆ average bond distance is ≈ 2.16 Å, the average bond distance for Sc(2)-O₇ is ≈ 2.20 Å with one long bond of 2.56 Å. The Sc(3)-O₇ polyhedron has an average bond length of approximately ≈ 2.20 Å. The scandium oxygen polyhedra are reasonably regular with only one long bond for Sc(2)-O. The average bond distances for Sc-O are all reasonably close to the expected values based on Shannon ionic radii $d(\text{Sc}^{3+}(\text{VI})-\text{O}) = 2.11$ Å and $d(\text{Sc}^{3+}(\text{VIII})-\text{O}) = 2.22$ Å⁴⁶. Vanadium is found in octahedral coordination with an average bond length of ≈ 1.97 Å for V(1)-O₆. It should be mentioned that one bond is very short with only 1.76 Å and one bond is about 2.23 Å long. The Shannon ionic radii for $d(\text{V}^{3+}(\text{VI})-\text{O}) = 1.99$ Å. The V(2)-O₄ tetrahedron has a bond length of 1.71912(8) Å which is too small for V⁴⁺. The bond length based on the Shannon radii $d(\text{V}^{4+}(\text{IV})-\text{O})$ is 1.93 Å for tetravalent vanadium in tetrahedral coordination. In contrast the bond distance as predicted by ionic radii is $d(\text{V}^{5+}(\text{IV})-\text{O}) = 1.71$ Å, this suggests that V⁵⁺ is possibly present in this structure.

Table 3-4: Bond distances for tetragonal Sc_2VO_5 from Rietveld refinement obtained from powder X-ray diffraction pattern with $\lambda = 1.540598 \text{ \AA}$, 1.544426 \AA .

Bonds (A-O)	Bond distance (\AA)
d (Sc(1)-O) (\AA)	2 * 2.352(5)
	2 * 2.020(7)
	2 * 2.109(7)
d (Sc(2)-O) (\AA)	2.092(9)
	2.190(8)
	2.215(9)
	2.012(9)
	2.234(8)
	2.095(8)
	2.560(8)
d (Sc(3)-O) (\AA)	2.251(9)
	2.124(8)
	2.291(8)
	2.032(8)
	2.222(8)
	2.088(8)
	2.386(9)
d (V(1)-O) (\AA)	1.971(9)
	1.933(9)
	1.967(10)
	1.956(10)
	1.755(9)
	2.230(9)
d (V(2)-O) (\AA)	4*1.71912(8)

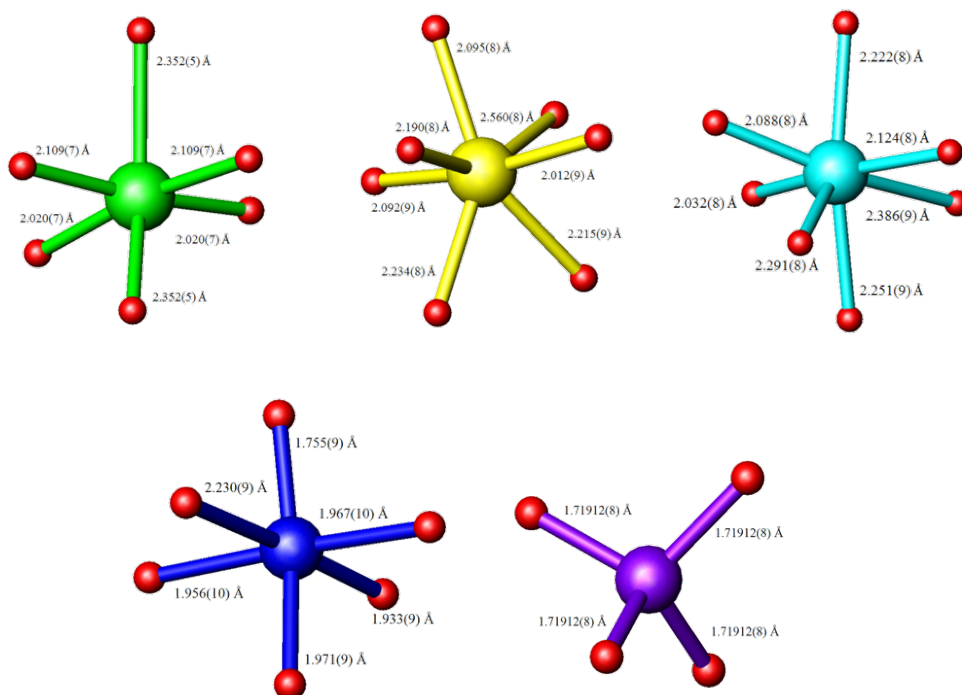


Figure 3-8: Illustration of local coordination environments and bond distances in tetragonal Sc_2VO_5 as discussed in the text. Green = Sc(1)-O₆, yellow = Sc(2)-O₇, turquoise = Sc(3)-O₇, dark blue = V(1)-O₆ and purple = V(2)-O₄.

The current Rietveld refinement does not support a more detailed structure analysis. However the structure of Sc_2VO_5 requires re-evaluation in terms of vanadium oxidation states. It is likely that V^{3+} and V^{5+} coexist in this structure which will also require some scandium-vanadium disorder on the remaining cation sites. X-ray diffraction alone with its similar form factors for scandium and vanadium is not appropriate for such an in-depth analysis. In the future combined powder neutron and powder X-ray diffraction data should be analysed in order to refine the cation occupancies and to further investigate the oxide sublattice. Unfortunately no samples of sufficient size for neutron powder diffraction are available to date. The current analysis strongly supports that the Sc_2VO_5 phase is the ordered tetragonal defect fluorite structure and that this phase can be prepared as a powder sample at 800°C in traces of O₂.

A number of different models for vanadium oxidation states need to be considered for this case. If V^{5+} is populating the $2d$ site then an equivalent amount of V^{3+} should be present e.g in the $8d$ vanadium site. The proposed model with only V^{5+} on the $2d$ site would also require an equivalent amount of V^{3+} to occupy for example the $8g$ site. In addition, V^{4+} would be present in the $8g$ site as well (i.e.: $8g$ site: 25% V^{3+} + 75% V^{4+}). This assumes that no vanadium/scandium mixing occurs. If any of the vanadium is located on any of the three scandium sites, a number of different charge distributions are feasible. XPS experiments were carried out, but did not provide any conclusive results. In order to answer the questions regarding the oxidation states of vanadium in Sc_2VO_5 XANES experiments are required. XANES is an oxidation state sensitive method since the method is dependent on the local environment of the atoms/ions. Changing the oxidation state leads to a change of the absorption edge energy. In order to address the mixing of vanadium and scandium multiple independent powder diffraction experiments would be required. In particular, neutron powder diffraction would be of value but in addition to the non-resonant powder X-ray diffractogram resonant X-ray diffraction experiments would be helpful.

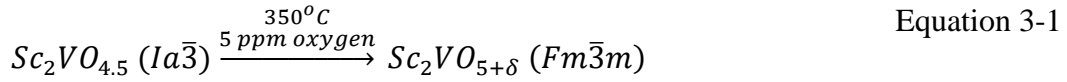
3.4 *In-situ* Diffraction Studies of Sc_2VO_5 Formation in O_2 Traces

The formation of the ordered tetragonal defect fluorite structure Sc_2VO_5 was further investigated by *in-situ* powder X-ray diffraction. It should be noted that the temperatures and reaction times cannot be directly compared between a bulk synthesis and an *in-situ* powder X-ray diffraction experiment. This is primarily due to sample size, heating rates and gas volume differences between those experiments. However the *in-situ* diffraction experiments can clearly illustrate the reaction pathway and

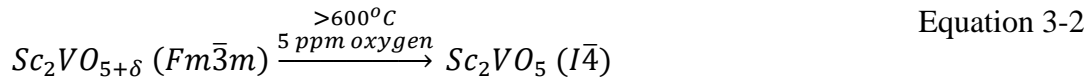
provide general guidelines for the preparation of bulk materials. The final bulk synthesis usually requires additional optimizations of the reaction conditions.

Figure 3-9 (a) shows a first insight into the *in-situ* oxidation of $\text{Sc}_2\text{VO}_{4.5}$ bixbyite in 5 ppm O_2 in N_2 during heating to 1200°C in 25°C increments and 1 min. data collection for each temperature step. The contour plot in Figure 3-9 (a) indicates the oxidation of the cation and oxide defect disordered $\text{Sc}_2\text{VO}_{4.5}$ bixbyite phase to the tetragonal Sc_2VO_5 structure at 600°C . This step involves (a) oxidation from V^{3+} to an average vanadium oxidation state of +4, (b) $\text{Sc}^{3+}/\text{V}^{4+}$ cation ordering (at least based on the current structural model for Sc_2VO_5) and (c) oxide defect ordering. Just below 1000°C the formation of ScVO_4 zircon is observed, indicating further oxidation of vanadium to V^{5+} . The stoichiometry requires the formation of Sc_2O_3 as a second product, unfortunately the peak overlap of Sc_2O_3 and Sc_2VO_5 prevents the observation of that phase. The tetragonal Sc_2VO_5 phase persists even up to 1200°C likely due to the limited amount of oxygen provided. The continuous decrease of the peak intensities for the Sc_2VO_5 phase highlights that the phase undergoes slow oxidation within the limit of accessible oxygen. The section 3-7 in this thesis explores and discusses details of the oxidation reaction in excess oxygen.

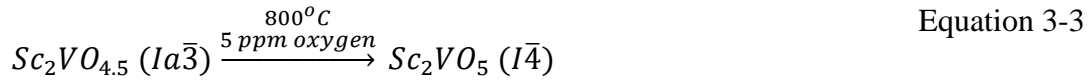
Particularly interesting are the details of the oxidation reaction illustrated in Figure 3-9 (b). The contour plot shows that a peak at $2\theta = 31.25^\circ$ starts to grow at 350°C . This peak is associated with the formation of the defect oxide fluorite phase $\text{Sc}_2\text{VO}_{5+\delta}$ (space group $Fm-3m$) with randomized oxide defects and a fully disordered cation lattice. This is a topotactic oxidation reaction which is commonly observed at low temperatures as only oxide anions are inserted into an otherwise unaltered structure¹³. Because of the limited amount of oxygen, only a small fraction of this phase is observed.



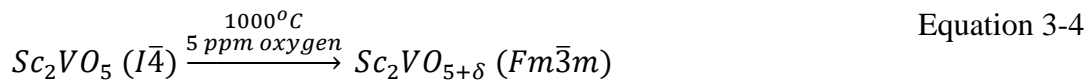
As more oxygen flows through the furnace and the temperature increases beyond 600°C, the defect fluorite structure undergoes a phase transition to the ordered tetragonal defect fluorite structure Sc_2VO_5 . There is no evidence of oxidation at that stage, this is a disorder-order transition.



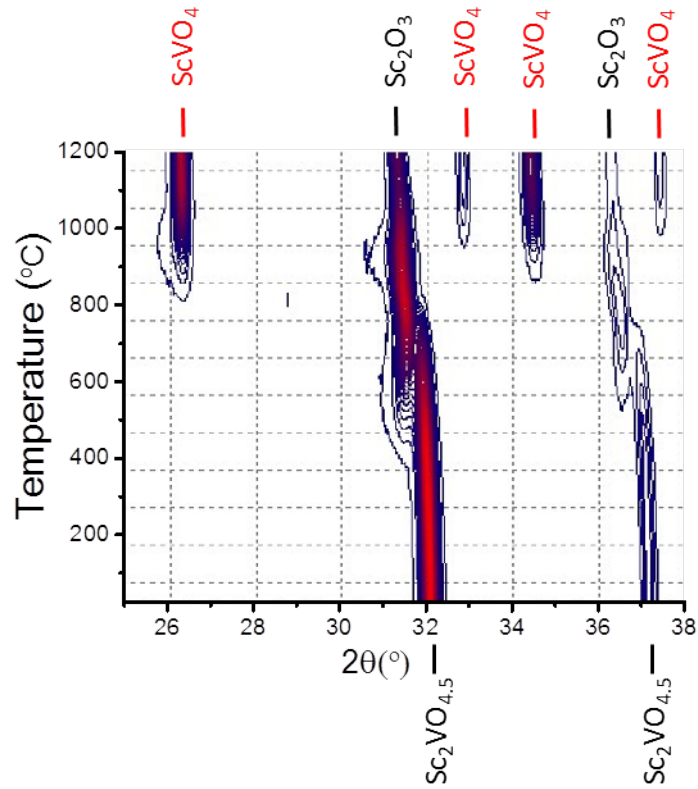
At even higher temperatures, about 800°C, the remaining bixbyite phase oxidizes directly to the cation ordered tetragonal structure. At that temperature the $Sc_2VO_{4.5}$ bixbyite peak vanishes in Figure 3-9 (b) and only the peak for the tetragonal phase is observed.



At approximately 1000°C the left peak in Figure 3-9 (b) broadens toward lower diffraction angles which is potentially an indication that Sc_2VO_5 undergoing yet another partial transformation to a defect fluorite phase.



(a)



(b)

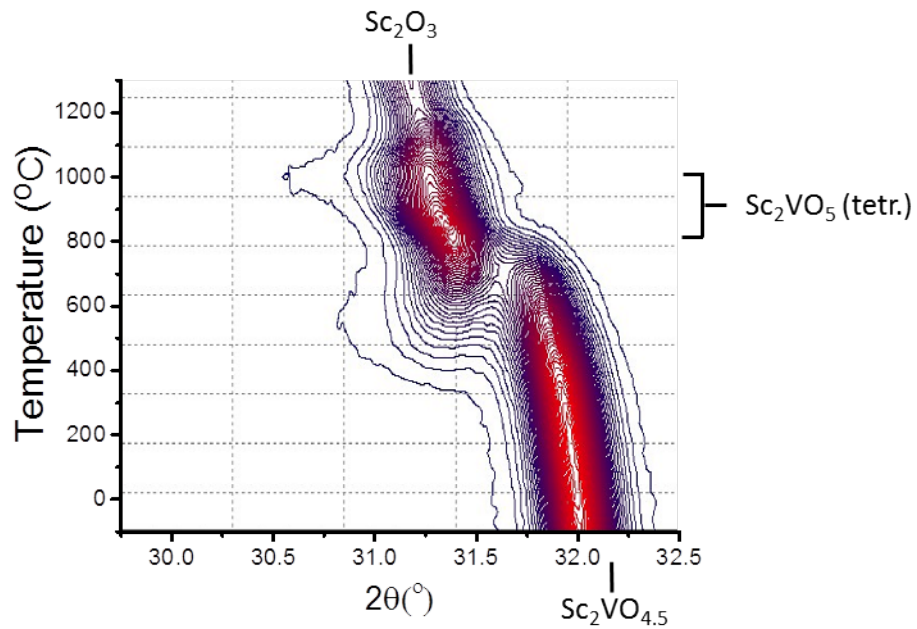
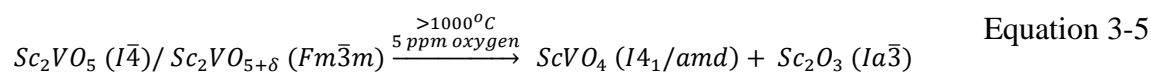


Figure 3-9: (a) High temperature powder X-ray diffraction contour plot following the oxidation of $\text{Sc}_2\text{VO}_{4.5}$ bixbyite in trace amount of oxygen from 25°C to 1200°C for $2\theta=18-65^{\circ}$. Data were collected in 25°C increments. (b) Selected range from 29.5° to 32.5° high temperature X-ray diffraction contour plot.

The phase mixture of the tetragonal Sc_2VO_5 and cubic defect fluorite $\text{Sc}_2\text{VO}_{5+\delta}$ eventually decomposes oxidatively into the ScVO_4 zircon phase and Sc_2O_3 bixbyite by-product.

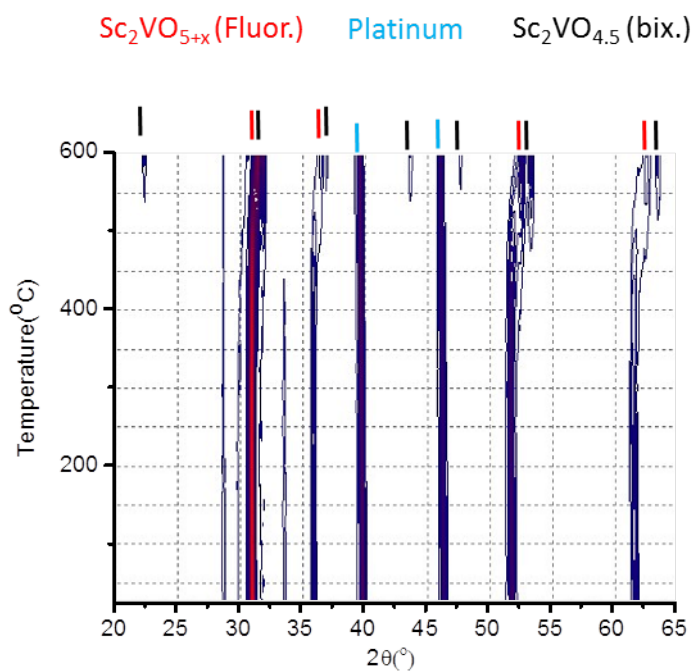


The details of the proposed oxidation pathway will be further explored in section 3-7 when comparing the oxidative stabilities of the disordered bixbyite and the ordered tetragonal phases in air using *in-situ* diffraction experiments.

3.5 Reductive Formation of Sc_2VO_5

The reductive synthesis of tetragonal Sc_2VO_5 was attempted using the defect fluorite phase $\text{Sc}_2\text{VO}_{5+\delta}$ ($0.00 \leq \delta \leq 0.50$) as a starting material. Figure 3-10 shows the contour plot of the high temperature *in-situ* powder X-ray diffraction study of the defect fluorite $\text{Sc}_2\text{VO}_{5+\delta}$ reduction in flowing hydrogen. Figure 3-10 (a) clearly illustrates the formation of the bixbyite phase at approximately 550°C as indicated by the appearance of the bixbyite superstructure peaks. Notably at 600°C the reduced bixbyite and the defect fluorite phase coexist. Figure 3-10 (b) shows sufficient detail of the reduction reaction to rule out the formation of an intermediate structure during the reduction in H_2 gas. The formation of the tetragonal form of Sc_2VO_5 is expected in dilute H_2 . More detailed studies are required to follow the potentially step-wise reduction in more depth. The reduction of bulk samples of the defect fluorite phase $\text{Sc}_2\text{VO}_{5+\delta}$ ($0.00 \leq \delta \leq 0.50$) in 3% hydrogen gas has produced the ordered tetragonal structure but only with large fractions of the bixbyite and fluorite phases present. Consequently the reduction of $\text{Sc}_2\text{VO}_{5+\delta}$ ($0.00 \leq \delta \leq 0.50$) might be feasible but is not a promising route for the preparation of phase-pure tetragonal Sc_2VO_5 .

(a)



(b)

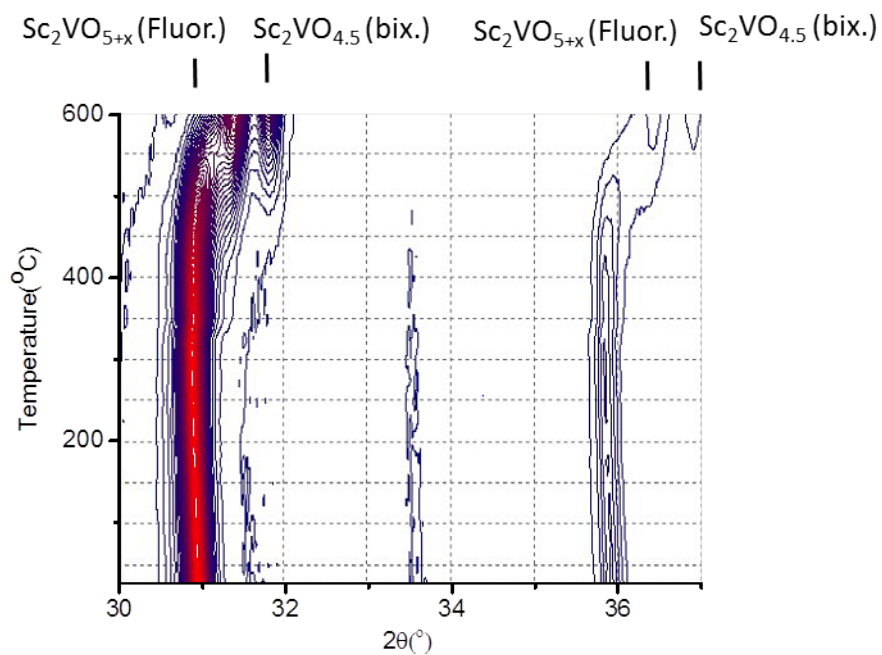
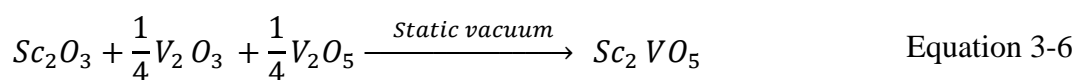


Figure 3-10: Contour plot of $\text{Sc}_2\text{VO}_{5+\delta}$ reduction in flowing H_2 during heating from 25 to 600°C with 25°C increments.

3.6 Solid State Direct Synthesis of Sc₂VO₅

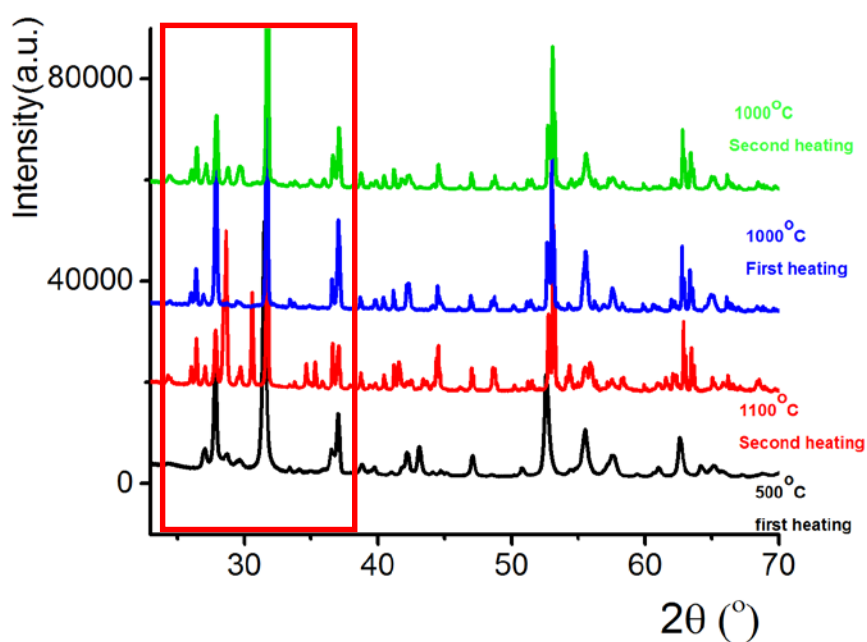
Mikhailov *et al.*³⁰ reported the shake and bake synthesis of tetragonal Sc₂VO₅ using stoichiometric amounts of Sc₂O₃ and VO₂ covering the temperature range from 700°C to 1200°C. Mikhailov *et al.* indexed the product on a different cell than Cong *et al.*²⁹ but likely formed the same structure. In an attempt to reproduce the early work of Mikhailov, the direct synthesis of tetragonal Sc₂VO₅ using stoichiometric amounts of Sc₂O₃, V₂O₃ and V₂O₅ was conducted. The reactions were carried out in a static vacuum according to Equation 3-6:



The temperatures for the conventional solid state synthesis ranged from 500°C to 1100°C. In Figure 3-11 the product obtained at 500°C is poorly crystalline, upon reheating the first product for 24 hours at 1100°C resulted in the tetragonal phase as the major product but significant amounts of monoclinic VO₂ (space group *P2₁/c*) and triclinic V₈O₁₅ (space group *P-1*) impurities are present. Even repeated heating at 1100°C did not form phase pure Sc₂VO₅. In Figure 3-11 stars indicate peaks belonging to the VO₂ phase and triangles refer to V₈O₁₅ phase. The large fractions of impurities formed during the conventional solid state synthesis method indicate that synthesizing the tetragonal Sc₂VO₅ phase by this method is not very promising.

The primary challenge of preparing tetragonal Sc₂VO₅ is the difficulty to obtain a single phase product. However it seems that Sc₂VO₅ is formed during all attempted synthesis attempts, i.e. during the topotactic oxidation, reconstructive oxidation, and reduction in dilute hydrogen and conventional solid state synthesis in static vacuum.

(a)



(b)

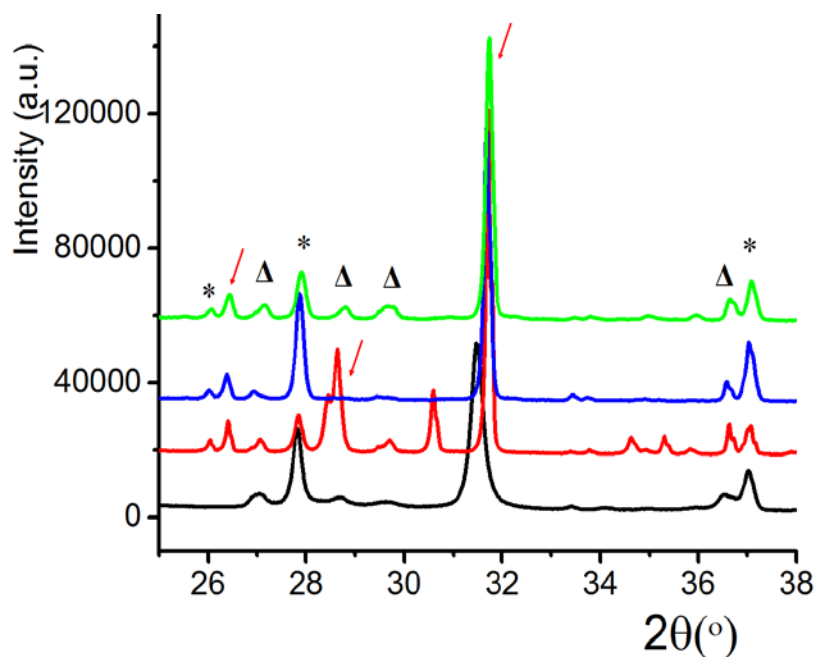


Figure 3-11: (a) Powder XRD patterns of Sc_2O_3 , V_2O_3 and V_2O_5 at 500°C in vacuum for first heating (black) and its second heating at 1100°C in vacuum (red). Blue pattern shows the first heating of another try at 1000°C in vacuum while the green diffractogram is the second heating at 1000°C . (b) Selected region of patterns to indicate the main phase is tetragonal Sc_2VO_5 (red arrows) and peaks marked with Stars represent monoclinic VO_2 and triangle marks are assigned to the V_8O_{15} phase.

3.7 *In-situ* High Temperature Oxidation of a Bi-phasic Sample of $\text{Sc}_2\text{VO}_{4.5}$ and Tetragonal Sc_2VO_5 in Air

In an effort to directly compare the oxidative stability of the bixbyite $\text{Sc}_2\text{VO}_{4.5}$ and the tetragonal Sc_2VO_5 phases, a phase mixture has been investigated by powder X-ray *in-situ* diffraction in air. The contour plot in Figure 3-12 (a) shows the oxidation of the bixbyite phase at 350°C as indicated by the disappearance of the $(222)_{\text{bix}}$ bixbyite peak and the appearance of the $(111)_{\text{fluor}}$ fluorite peak at the same temperature. The $(111)_{\text{fluor}}$ fluorite peak follows the previously reported gradual increase of d-spacing due to progressive oxygen uptake²⁴. This process is the topotactic oxidation of $\text{Sc}_2\text{VO}_{4.5}$ (bixbyite) to the $\text{Sc}_2\text{VO}_{5+\delta}$ ($0 < \delta \leq 0.5$) fluorite phase. The cubic space group symmetry changes from $Ia-3$ to $Fm-3m$ with the smaller fluorite cell. This finding is in agreement with the previous work reported by Shafi *et al*¹³. The $(123)_{\text{tet}}$ peak for the tetragonal Sc_2VO_5 phase does not show any changes other than thermal expansion up to approximately 700°C. This clearly illustrates the relative oxidative stability of the tetragonal Sc_2VO_5 phase with respect to the cubic $\text{Sc}_2\text{VO}_{4.5}$ bixbyite structure. The tetragonal phase also oxidizes to the defect fluorite structure but only at 700°C. This oxidation proceeds with an increase in symmetry from $I-4$ to $Fm-3m$. Since there is only one cation site accessible in the fluorite structure this oxidation must be accompanied by an order-disorder transition on the cation sublattice. The same argument holds for the anion sublattice where the oxide ions and oxide defects were ordered in the tetragonal phase but are disordered in the cubic fluorite phase because of only having one accessible anion site in space group $Fm-3m$.

The temperature range 600 to 900°C is particularly interesting. Figure 3-12 (b) shows the *in-situ* powder diffractograms. The data clearly indicate that the fluorite phase that was initially formed from the bixbyite phase has a larger unit cell constant (smaller

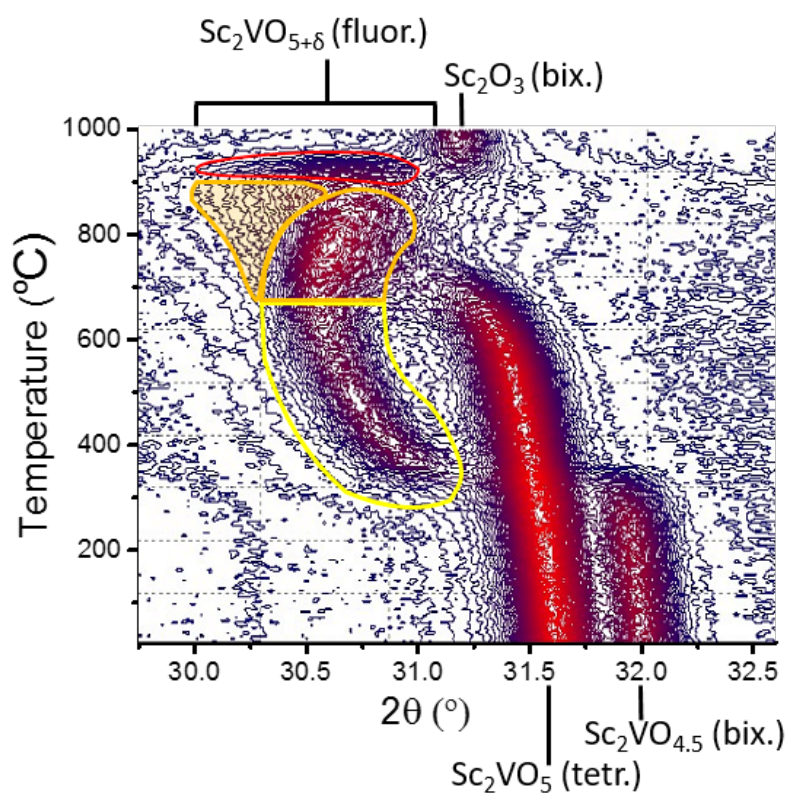
diffraction angle) than the fluorite phase formed from the tetragonal phase at 700°C. This clearly shows that the initial fluorite phase had undergone a large oxygen uptake whereas the Sc₂VO₅ phase seems to form a fluorite phase with less oxygen. Since the fluorite peak shifts to higher diffraction angles (smaller unit cell) between 700°C and 900°C it is suggested that oxygen is exchanged between the two fluorite phases with a resulting homogenization of the phase. This process can be expressed as:



Furthermore this suggests that the initially formed Sc₂VO_{5+δ} must have had an oxygen stoichiometry of > 5. The significant broadening of the fluorite (111) peak around 900°C suggests an amorphization of the defect fluorite structure during further oxidation. The peak broadening is emphasized in Figure 3-12 (b) as well. At approximately 950°C the formation of the pentavalent zircon phase ScVO₄ and the bixbyite by-product Sc₂O₃ is observed.

When oxidizing Sc₂VO₅ the ScVO₄ zircon structure is observed about 200°C above the temperature observed for the formation of ScVO₄ from ScVO₃²². It is proposed that the oxidative phase separation of Sc₂VO₅ into ScVO₄ and Sc₂O₃ requires a higher temperature than the phase transition from ScVO_{3.5+x} to ScVO₄ without phase separation. This is illustrated in Figure 3-12.

(a)



(b)

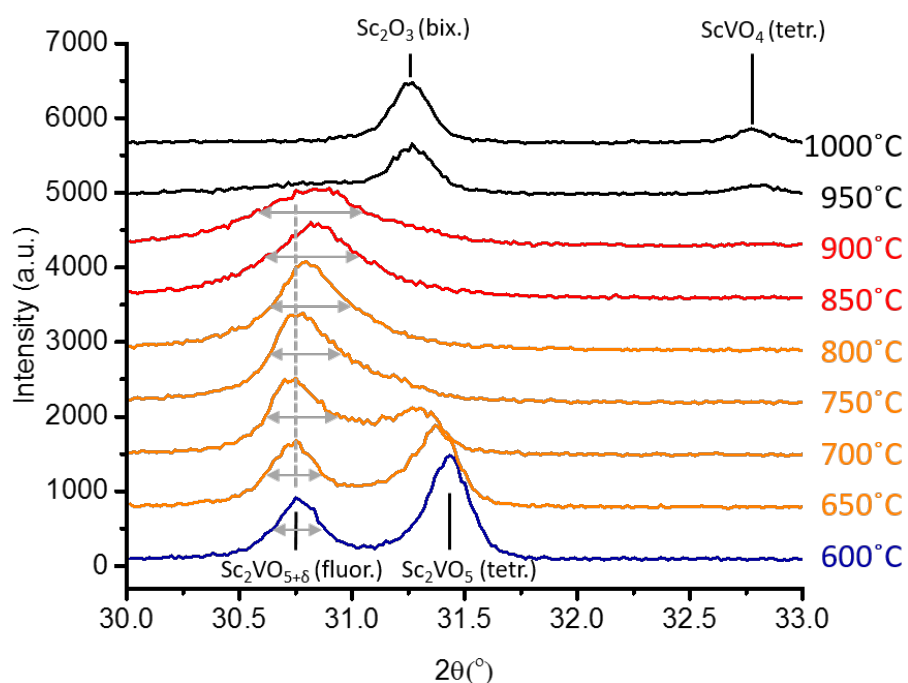


Figure 3-12: (a) High temperature powder X-ray diffraction contour plot following the oxidation of $\text{Sc}_2\text{VO}_{4.5}$ bixbyite and the tetragonal Sc_2VO_5 . Data were collected in 5°C increments. (b) Individual in-situ powder X-ray diffractograms between 600°C and 1000°C emphasizing the phase evolution during oxidation in air. The grey double headed arrows emphasize the peak broadening for the fluorite phase up to 900°C . All relevant phases are indicated in figures 3-5 (a) and (b).

The oxidation of the $\text{Sc}_2\text{VO}_{4.5}$ bixbyite and Sc_2VO_5 tetragonal phase mixture has also been investigated by *in-situ* powder X-ray diffraction using only traces of oxygen. By limiting the available oxygen while using the same heating rate the two phases now compete for the oxygen. The drastic peak shift for the oxidation of the bixbyite to defect fluorite structure as observed in Figure 3-12 indicates that a large amount of oxygen is required for the formation of the defect fluorite structure.

The contrasting reaction of the phase mixture $\text{Sc}_2\text{VO}_{4.5}$ (bix.) and Sc_2VO_5 (tetr.) in traces of oxygen is illustrated in the powder X-ray *in-situ* diffraction experiment in Figure 3-13.

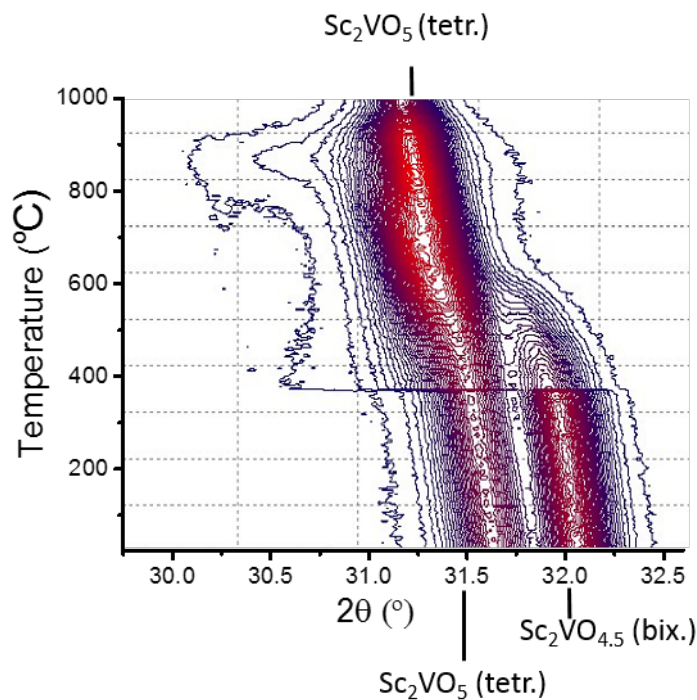


Figure 3-13: High temperature powder X-ray diffraction contour plot following the oxidation of $\text{Sc}_2\text{VO}_{4.5}$ bixbyite and the tetragonal Sc_2VO_5 in trace amount of oxygen from 25°C to 1000 °C. Data were collected in 5°C increments. The step at 370 °C is an experimental artifact due to an unexpected hold time at that temperature.

The oxidation in traces of oxygen shows the slow disappearance of the $(222)_{\text{bix}}$ bixbyite peak at approximately 500°C with no apparent appearance of the characteristic low angle $(111)_{\text{fluor}}$ fluorite peak. Instead the intensity of the $(123)_{\text{tet}}$ peak belonging to the Sc_2VO_5 phase increases. Consequently with insufficient oxygen the bixbyite phase undergoes slow oxidation to the ordered Sc_2VO_5 tetragonal phase. This can be explained with the competition of a kinetic pathway that permits the formation of the fluorite structure if sufficient oxygen is available, whereas an insufficient amount of oxygen will favor the gradual high temperature pathway toward the cation ordered tetragonal Sc_2VO_5 phase. Figure 3-13 also shows the onset of another phase above 950°C . The evolving peak is in agreement with the formation of Sc_2O_3 but unfortunately the data are not of sufficient quality to confirm that this is indeed $\text{ScVO}_4 + \frac{1}{2} \text{Sc}_2\text{O}_3$ formation.

Chapter 4

CONCLUSION

The purpose of this thesis is to study structure-reactivity relationships for the Sc-V-O system as well as investigation of bixbyite, defect fluorite, and tetragonal phases. In addition, phase changes or phase boundaries have been studied along with the identification of present phases. Investigation of the reaction pathway of the aforementioned structures by means of *in-situ* and *ex-situ* powder X-ray diffraction is one of the important outcomes of this study.

Special attention has been given to the comparison of thermodynamically and kinetically favored products. The structure related properties for the Sc-V-O system oxidation and reduction pathway have been studied and the *in-situ* diffraction experiments were used to explore the oxidation sequence. The redox cycle for $\text{Sc}_2\text{VO}_{4.5}$ – ScVO_4 as well as $\text{Sc}_2\text{VO}_{4.5}$ – Sc_2VO_5 were investigated for their structures and stability. The phase change of cation-disordered bixbyite $\text{Sc}_2\text{VO}_{4.5}$ to cation-ordered tetragonal Sc_2VO_5 has been studied through oxidation in trace amount of oxygen. Moreover, the oxidation of bi-phasic samples of $\text{Sc}_2\text{VO}_{4.5}$ and Sc_2VO_5 clearly supports the competition of thermodynamic and kinetic products.

In Figure 4-1 the relation between reaction temperatures and obtainable structures during the *ex-situ* oxidation in trace amounts of oxygen is shown. Oxidation processes are

illustrated with arrows and products are indicated inside the rectangular boxes. The temperature is indicated on the y-axis. The Sc-V-O phases can be explained with three different oxidation states of vanadium; V^{3+} in $Sc_2VO_{4.5}$, V^{4+} in Sc_2VO_5 and V^{5+} in the $ScVO_4$ zircon phase and the $Sc_2VO_{5+\delta}$ fluorite phase.

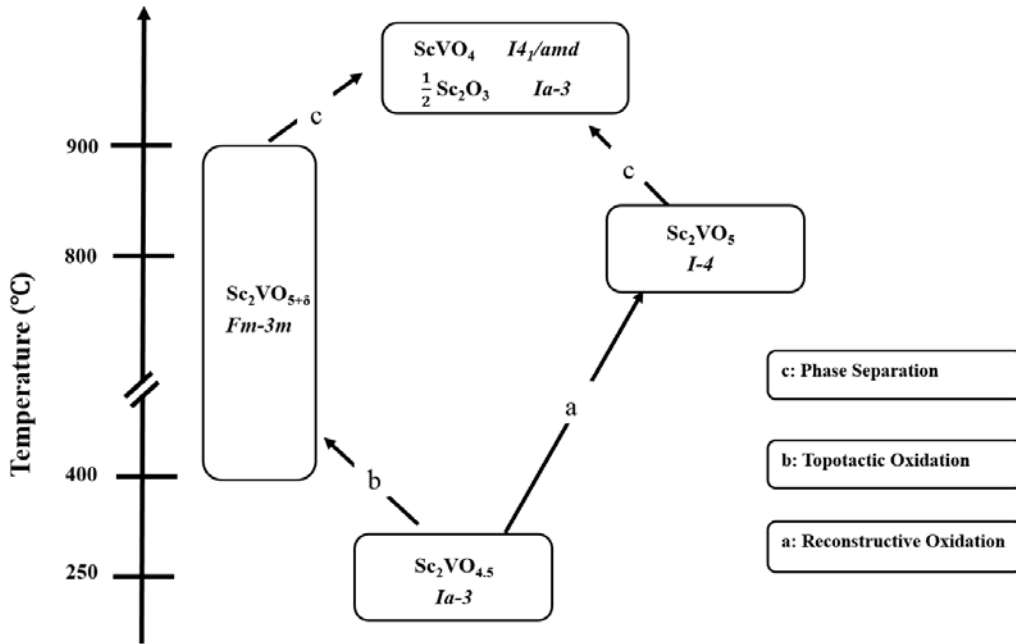


Figure 4-1: Flow chart of oxidation pathways for the Sc-V-O system as a function of temperature in trace amounts of oxygen as determined from ex-situ oxidation experiments starting with the $Sc_2VO_{4.5}$ bixbyite phase.

In conclusion, the reported results indicate the formation of two different products at two different temperatures when oxidizing in the presence of enough oxygen. One product is the thermodynamically stable phase while the second pathway results in a kinetically favorable product. At $\sim 800^\circ\text{C}$ the dominant product is the tetragonal Sc_2VO_5 phase (thermodynamically stable product). This phase can only be obtained at high temperature in traces of oxygen. Ideally no oxygen should be supplied before the reaction temperature

of 800°C has been reached. During its formation, the bixbyite phase undergoes a slow reconstructive oxidation to the ordered tetragonal Sc_2VO_5 structure.

In contrast, the kinetic oxidation product of $\text{Sc}_2\text{VO}_{4.5}$ bixbyite is obtained at temperatures as low as $\approx 400^\circ\text{C}$. The topotactic pathway involves the insertion of oxygen into the bixbyite lattice without reconstructing the cation sublattice. Consequently, the disordered cation sublattice of the bixbyite phase remains and acts as the disordered fluorite cation sublattice. In the fluorite structure only one oxygen site is available and consequently oxide anions and oxide defects are randomized on this single site. A temperature of only 400°C does not provide sufficient thermal energy for a reconstructive process. Furthermore the topotactic oxidation is a fast process that is only limited by oxide diffusion.

The reactivities of the most important phases has been further investigated in air. This assures that the reactions are not oxygen limited. The simultaneous *in-situ* oxidation in air of the $\text{Sc}_2\text{VO}_{4.5}$ bixbyite phase and the tetragonal Sc_2VO_5 structure clearly showed that the topotactic oxidation of the bixbyite phase to the defect fluorite phase occurs already at $\approx 400^\circ\text{C}$. The tetragonal phase does not react until a temperature of $\sim 800^\circ\text{C}$ has been reached. The high temperature is required in order to overcome the high activation energy of reconstructing the cation sublattice. Figure 4-2 schematically illustrates the presence of the different phases as a function of temperature during oxidation in excess oxygen. The tetragonal Sc_2VO_5 phase undergoes further oxidation to the cubic defect fluorite phase $\text{Sc}_2\text{VO}_{5+\delta}$ ($0.00 \leq \delta \leq 0.50$). During this step the cations undergo disorder and further oxidation is enabled by permitting the coexistence of V^{4+} and V^{5+} in this disordered

structure. Beyond 900°C the cubic defect fluorite structure $\text{Sc}_2\text{VO}_{5+\delta}$ collapses and undergoes phase separation into zircon ScVO_4 and bixbyite Sc_2O_3 products.

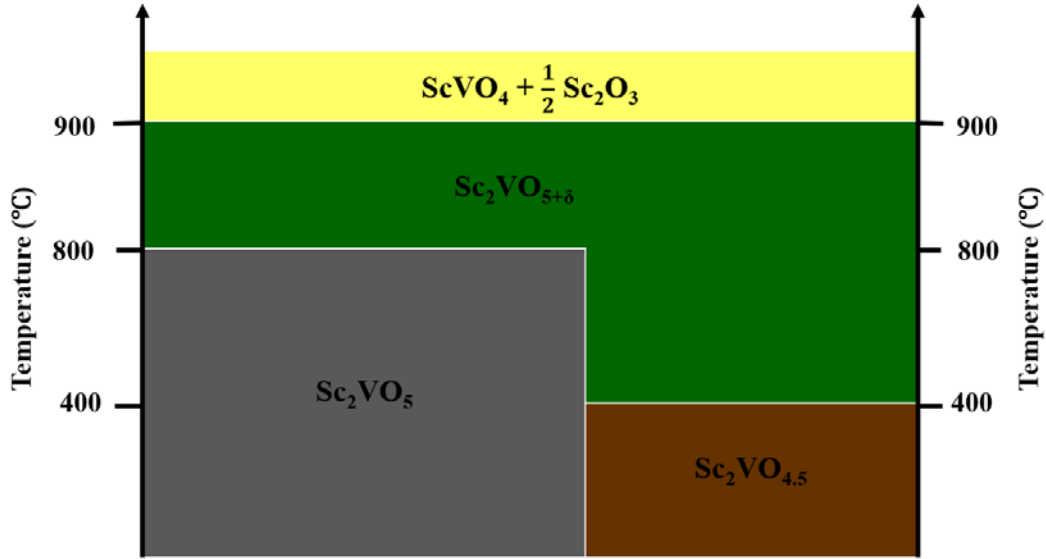


Figure 4-2: Phase existence as observed during the in-situ oxidation in air of a biphasic $\text{Sc}_2\text{VO}_{4.5}$ bixbyite and tetragonal Sc_2VO_5 sample. The intermediate phase is the $\text{Sc}_2\text{VO}_{5+\delta}$ fluorite phase and the final products are the ScVO_4 zircon structure and the Sc_2O_3 bixbyite structure.

In this thesis the Sc-V-O system was used as a model for solid state electrolytes for solid oxide fuel cell applications. The research does not only shed light on the structure-reactivity relationship but also illustrates the structural versatility within the Sc-V-O system. Moreover, the synthesis and characterization will hopefully provide a larger tool set for optimizing synthesis strategies in particular for the Sc-V-O system. Future work should be based on the further findings when exploring other members of the A_2VO_5 family. Sc_2VO_5 should be investigated by neutron powder diffraction and XANES in particular.

REFERENCES

- (1) Minh, N. Q. *Solid State Ionics* **2004**, *174* (1-4), 271–277.
- (2) Yamamoto, O. *Electrochim. Acta* **2000**, *45*, 2423–2435.
- (3) Kharton, V. V.; Marques, F. M. B.; Atkinson, A. *Solid State Ionics* **2004**, *174* (1-4), 135–149.
- (4) Skinner, S. J.; Kilner, J. A. *Mater. Today* **2003**, *6* (3), 30–37.
- (5) Singhal, S. C. *Solid State Ionics* **2000**, *135*, 305–313.
- (6) Fergus, J. W. *J. Power Sources* **2006**, *162*, 30–40.
- (7) Marques, F. M. B.; Kharton, V. V.; Naumovich, E. N.; Shaula, A. L.; Kovalevsky, A. V.; Yaremchenko, A. A. *Solid State Ionics* **2006**, *177* (19), 1697–1703.
- (8) Kilner, J. A. *Solid State Ionics* **2000**, *129* (1), 13–23.
- (9) Hryha, E.; Rutqvist, E.; Nyborg, L. *Surf. Interface Anal.* **2012**, *44* (8), 1022–1025.
- (10) Heifets, E.; A., E.; A., Y.; Piskunov, S.; Maier, J. In *Thermodynamics - Interaction Studies - Solids, Liquids and Gases*; InTech, **2011**.
- (11) Giaquinta, D. M.; zur Loye, H.-C. *Chem. Mater.* **1994**, *6* (4), 365–372.
- (12) Aughterson, R. D.; Lumpkin, G. R.; Thorogood, G. J.; Zhang, Z.; Gault, B.; Cairney, J. M. *J. Solid State Chem.* **2015**, *227*, 60–67.
- (13) Shafi, S. P.; Lundgren, R. J.; Cranswick, L. M. D.; Bieringer, M. *J. Solid State Chem.* **2007**, *180* (12), 3333–3340.
- (14) Chroneos, A.; Vovk, R. V.; Goulatis, I. L.; Goulatis, L. I. *J. Alloys Compd.* **2010**, *494* (1-2), 190–195.
- (15) Mainz, U. *Ionics (Kiel)*. **1996**, *85*, 25–35.
- (16) Johnsson, M.; Lemmens, P. *John Wiley Sons, Ltd., New York* **2007**, 11.

- (17) Lufaso, M. W.; Woodward, P. M. *Acta Crystallogr. Sect. B Struct. Sci.* **2004**, *60* (1), 10–20.
- (18) Aso, R.; Kan, D.; Shimakawa, Y.; Kurata, H. *Sci. Rep.* **2013**, *3*, 2214.
- (19) Li, Z.; Yang, M.; Park, J. S.; Wei, S. H.; Berry, J. J.; Zhu, K. *Chem. Mater.* **2016**, *28* (1), 284–292.
- (20) Shafi, S. P. Solid State Structure-Reactivity Studies on Bixbyites, Fluorites and Perovskites Belonging to the Vanadate, Titanate and Cerate Families., University of Manitoba, 2012.
- (21) Alonso, J. A.; Casais, M. T.; Mart'inez-Lope, M. J. *Dalton Trans.* **2004**, No. 9, 1294–1297.
- (22) Shafi, S. P.; Kotyk, M. W.; Cranswick, L. M. D.; Michaelis, V. K.; Kroeker, S.; Bieringer, M. *Inorg. Chem.* **2009**, *48* (22), 10553–10559.
- (23) Lundgren, R. J.; Cranswick, L. M. D.; Bieringer, M. *J. Solid State Chem.* **2006**, *179* (12), 3599–3606.
- (24) Lussier, J. A.; Szkop, K. M.; Sharma, A. Z.; Wiebe, C. R.; Bieringer, M. *Inorg. Chem.* **2016**, acs.inorgchem.5b02746.
- (25) Lussier, J. A.; Devitt, G.; Szkop, K. M.; Bieringer, M. *J. Solid State Chem.* **2016**.
- (26) Dorogova, M.; Navrotsky, A.; Boatner, L. A. *J. Solid State Chem.* **2007**, *180* (3), 847–851.
- (27) Hayun, S.; Navrotsky, A. *J. Solid State Chem.* **2012**, *187*, 70–74.
- (28) Gao, X.; Ruiz, P.; Xin, Q.; Guo, X.; Delmon, B. *Catal. Letters* **1994**, *23* (3-4), 321–337.
- (29) Cong, H.; Zhang, H.; Yao, B.; Yu, W.; Zhao, X.; Wang, J.; Zhang, G. *Cryst. Growth Des.* **2010**, *10* (10), 4389–4400.
- (30) Komissarova, L. .; Mikhailov., Y. Y.; Pokrovskii, B. . *Dokl. Chem.* **1971**, *193*, 403.

- (31) Senegas, P. A. R. J.; Et, J. M.; Galy, J. *Acta Cryst. (1975)*. **1975**, B31, 1614–1618.
- (32) Singh, Y.; McCallum, R.; Johnston, D. *Phys. Rev. B* **2007**, 76 (17), 174402.
- (33) Taetz, T.; Hollmann, N.; Mydosh, J. a; Kataev, V.; Yehia, M.; Vavilova, E. **2011**, 1–10.
- (34) Whittle, K. R.; Blackford, M. G.; Aughterson, R. D.; Lumpkin, G. R.; Zaluzec, N. *J. Acta Mater.* **2011**, 59 (20), 7530–7537.
- (35) Tracy, C. L.; Lang, M.; Zhang, J.; Zhang, F.; Wang, Z.; Ewing, R. C. *Acta Mater.* **2012**, 60 (11), 4477–4486.
- (36) Zhang, J.; Zhang, F.; Lang, M.; Lu, F.; Lian, J.; Ewing, R. C. *Acta Mater.* **2013**, 61 (11), 4191–4199.
- (37) Kimani, M. M.; McMillen, C. D.; Kolis, J. W. *Inorg. Chem.* **2012**, 51 (6), 3588–3596.
- (38) Hagemuller, P. *Preparative methods in solid state chemistry*; Academic Press, **1972**.
- (39) Schaeffer, R. W. *J. Chem. Educ.* **2000**, 77 (7), 833.
- (40) Stanjek, H.; Häusler, W. *Hyperfine Interact.* **2004**, 154 (1-4), 107–119.
- (41) McCusker, L. B.; Von Dreele, R. B.; Cox, D. E.; Louër, D.; Scardi, P. *J. Appl. Crystallogr.* **1999**, 32 (1), 36–50.
- (42) Lundgren, R. J.; Cranswick, L. M. D.; Bieringer, M. **2007**, 3 (4), 3945–3955.
- (43) Fallis, A. . *Clim. Chang. 2013 - Phys. Sci. Basis* **2012**, 53 (9), 1–30.
- (44) Stephens, P. W. **2012**, 15–26.
- (45) Young, R. A. (Robert A. *The Rietveld method*; International Union of Crystallography, **1993**.
- (46) Radii, S. Database of Ionic Radii <http://abulafia.mt.ic.ac.uk/shannon/ptable.php>.

(47) West, A. R. *Solid State Chemistry and Its Applications*; **1991**.